



Enhanced Abyssal Mixing in the Equatorial Pacific Associated with Non-Traditional Effects

Bertrand L. Delorme* and Leif N. Thomas

Earth System Science Department, Stanford University, Stanford, California

Patrick Marchesiello

IRD/LEGOS, Toulouse, France

Jonathan Gula

*Univ. Brest, CNRS, IRD, Ifremer, Laboratoire d'Océanographie Physique et Spatiale (LOPS),
IUEM, Brest, France, and Institut Universitaire de France (IUF)*

Guillaume Roullet

*Univ. Brest, CNRS, IRD, Ifremer, Laboratoire d'Océanographie Physique et Spatiale (LOPS),
IUEM, Brest, France*

M. Jeroen Molemaker

*Department of Atmospheric and Oceanic Sciences, University of California Los Angeles, Los
Angeles, California*

*Corresponding author address: Bertrand Delorme, Stanford University, 473 Via Ortega, Stanford,
CA 94305

¹⁸ E-mail: bdelorme@stanford.edu

ABSTRACT

Recent theoretical work has shown that, when the so-called non-traditional effects are taken into account, the reflection of Equatorially Trapped Waves (ETWs) off the seafloor generates strong vertical shear that results in bottom-intensified mixing at the inertial latitude of the ETW via a mechanism of critical reflection. It has been estimated that this process could play an important role in driving diapycnal upwelling in the Abyssal Meridional Overturning Circulation (AMOC). However, these results were derived under an idealized configuration with a monochromatic ETW propagating through a flat ocean at rest. To test the theory in a flow that is more representative of the ocean, we contrast a set of realistic numerical simulations of the Eastern Equatorial Pacific run using either the hydrostatic or quasi-hydrostatic approximation, the latter of which accounts for non-traditional effects. The simulations are nested into a Pacific-wide hydrostatic parent solution forced with climatological data and realistic bathymetry, resulting in an ETW field and a deep circulation consistent with observations. Using these simulations, we observe enhanced abyssal mixing in the quasi-hydrostatic run, even over smooth topography, that is absent in the hydrostatic run. The mixing is associated with inertial shear that has spatio-temporal properties consistent with the critical reflection mechanism. The enhanced mixing results in a weakening of the abyssal stratification and drives diapycnal upwelling in our simulation, in agreement with the predictions from the idealized simulations. The diapycnal upwelling is on the order of $O(10)$ Sv and thus could play an important role in closing the AMOC.

⁴² **1. Introduction**

⁴³ The Abyssal Meridional Overturning Circulation (AMOC) is associated with production of
⁴⁴ abyssal waters through deep convection around Antarctica. Consequently, mixing processes are
⁴⁵ required to lift the abyssal waters back up and eventually close the AMOC. Although the polar
⁴⁶ source regions of abyssal waters have been identified, the energy sources driving mixing and their
⁴⁷ spatio-temporal distribution are still a subject of debate (Ferrari 2014). More than a decade ago,
⁴⁸ inverse calculations from Lumpkin and Speer (2007) showed that much of the zonally integrated
⁴⁹ diapycnal upwelling that closes the AMOC occurs in the tropical oceans, suggesting that intense
⁵⁰ mixing takes place in these regions. However, we lack both observational evidence and robust
⁵¹ theories that could support the inferences from these inverse models.

⁵² In a recent paper, Delorme and Thomas (2019) (hereafter DT19) showed that surface-generated
⁵³ Equatorially Trapped Waves (ETWs) can energize mixing in the abyss of the tropical oceans upon
⁵⁴ reflection off the seafloor when the full Coriolis force and so-called non-traditional (NT) effects are
⁵⁵ taken into account. DT19 used an idealized model configuration where the horizontal component
⁵⁶ of the Earth's rotation, \tilde{f} , is non-zero, allowing for NT effects to be triggered. Their domain
⁵⁷ consists of an equatorial channel with a flat bottom and periodic zonal boundary conditions. At
⁵⁸ the surface, monochromatic downward-propagating ETWs are generated in a 1-km thick sponge
⁵⁹ layer and propagate freely in the deep within an ocean at rest. Once they reach the weakly stratified
⁶⁰ abyss, all types of ETWs – from Inertia-Gravity Waves (IGWs) to Rossby waves – are modified by
⁶¹ the NT effects, and they ultimately undergo critical reflection at their inertial latitude where their
⁶² frequency equals the local inertial frequency, f . The critical reflection mechanism is triggered
⁶³ by a change in the meridional scale of the reflected waves: NT effects act to break the vertical
⁶⁴ symmetry of downward-propagating ETWs, and, by so doing, they yield a more complex bottom

65 reflection that requires higher meridional modes to satisfy the boundary conditions. These higher
66 meridional modes are governed by a two-dimensional wave equation for IGWs with NT terms that
67 predicts the occurrence of critical reflection at the inertial latitude of the wave (Gerkema and Shrimpton
68 2005; Winters et al. 2011). This process acts to locally enhance the shear, which drives mixing
69 in DT19's simulations. Although the mixing is confined to the inertial latitude, DT19 estimated
70 that it could drive large-scale diapycnal upwelling to the order of 10 Sv and thus significantly
71 contribute to closing the AMOC.

72 However, DT19's prediction was derived from a highly idealized configuration that has five po-
73 tential limitations. First, DT19 only considered single monochromatic waves, whereas the equa-
74 torial ocean consists of a spectrum of waves. Second, the forcing mechanism in DT19 is zonally
75 symmetric and persistent in time, yielding persistent and zonally uniform mixing. In the real
76 ocean, downward-propagating ETWs are generated at the surface through winds (Kessler and Mc-
77 Creary 1993; Kelly et al. 1995; Durland and Farrar 2012) and through upper-ocean instabilities
78 associated with western boundary currents, Tropical Instability Waves (TIWs), or the equatorial
79 undercurrent (Kindle and Thompson 1989; Woodberry et al. 1989; Asciani et al. 2010). Such forc-
80 ing mechanisms exhibit zonal and meridional variations as well as temporal variability, which
81 ultimately manifest in the ETW field. For example, TIWs occur predominantly on the eastern side
82 of the ocean basin with most of their energy confined primarily north of the Equator (Malardé
83 et al. 1987), and they occur mostly between August and December (Qiao and Weisberg 1995). Ir-
84 regular forcing patterns might lead to areas or periods where most of the waves' energy converges
85 at depth, but also to "shadow zones" where the waves' energy is very weak or episodic. Third, the
86 stratification in DT19's model is horizontally uniform. Horizontal variations in the stratification
87 in the real ocean might have a strong influence on DT19's theory at depth since NT effects are
88 strongly dependent on the value of the bottom stratification. Fourth, the wave in DT19's model

89 propagates in an ocean at rest, whereas the equatorial ocean is known for having a very energetic
90 circulation at depth with the presence of the so-called Equatorial Deep Jets (Cravatte et al. 2017;
91 Méneguen et al. 2019). Fifth and last, the bathymetry in DT19's configuration is flat. The non-flat
92 bathymetry in the real ocean can affect the occurrence and intensity of critical reflection, an effect
93 that also needs to be investigated.

94 In this study, our primary goal is to address these potential limitations by investigating how
95 DT19's theory may manifest itself in the real ocean. We would like to know where and when
96 critical reflection due to NT effects should be expected, and what are its effects on abyssal mixing
97 and stratification in the equatorial oceans. To answer these questions, we focus on the Eastern
98 Equatorial Pacific ocean, using a set of two realistic, high-resolution simulations with and without
99 \tilde{f} . These simulations are driven by climatological forcing and use a grid nesting approach from
100 a parent, basin-wide simulation of the Pacific Ocean. A comparison of the simulations with and
101 without \tilde{f} allows us to investigate the influence of NT effects on the properties of the abyssal
102 equatorial ocean.

103 The remainder of this paper is organized as follows. The numerical model and simulation setup
104 are described in section 2. A comparison of the simulations with and without \tilde{f} is presented in
105 section 3 to highlight the key differences that we observe in the abyssal ocean with NT effects.
106 These differences are interpreted with the theory for critical reflection that has been predicted by
107 DT19 in section 4, and the implications for diapycnal transport in the abyss are discussed. The
108 article is concluded in section 5 with a discussion of the strengths and limitations of the theory and
109 potential topics for future research.

¹¹⁰ **2. Model setup**

¹¹¹ In this section, we introduce the realistic simulations of the Pacific ocean run with two regional
¹¹² models based on the Regional Oceanic Modeling System (ROMS; Shchepetkin and McWilliams
¹¹³ 2005, 2009). ROMS solves the primitive equations for the velocity, potential temperature, and
¹¹⁴ salinity, using a full equation of state for seawater (Shchepetkin and McWilliams 2008, 2011).

¹¹⁵ We used a one-way nesting procedure to go from a parent grid covering most of the Pacific
¹¹⁶ Ocean to a child grid centered around the Eastern Equatorial Pacific. The two successive domains
¹¹⁷ are highlighted in Figure 1a, which shows a snapshot of the Sea Surface Temperature (SST) from
¹¹⁸ the model. One-way nesting has been used with success in the past to obtain local solutions at high
¹¹⁹ resolution while preserving the regional-scale circulation (Penven and Debreu 2006; Mason et al.
¹²⁰ 2010; Molemaker et al. 2015; Gula et al. 2015). In this configuration, there is no feedback from the
¹²¹ child grid to the parent grid: the parent simulation supplies only boundary and initial conditions
¹²² to the child simulation offline, and each simulation is run independently. The boundary condition
¹²³ algorithm that we used consists of a modified Flather-type scheme for the barotropic mode (Mason
¹²⁴ et al. 2010) and an Orlanski-type scheme for the baroclinic mode (Marchesiello et al. 2001).

¹²⁵ In our study, the parent simulation was run with the UCLA version of the ROMS model, while
¹²⁶ the child simulation was run with the CROCO version of the ROMS model (see Jullien et al. 2019,
¹²⁷ section 16.3, for a thorough description of the different versions of ROMS and their historical de-
¹²⁸velopment). We used the CROCO version because it has been recently enhanced with the addition
¹²⁹ of a Quasi-Hydrostatic (QH) option. The QH equations do not include the vertical acceleration but
¹³⁰ do take into account the NT terms (i.e., $\tilde{f}w$ in the zonal momentum equation and $\tilde{f}u$ in the vertical
¹³¹ momentum equation, the latter of which modifies the hydrostatic pressure field, and where (u, v, w)
¹³² is the velocity vector). Appendix A describes the QH implementation of CROCO in more detail,

¹³³ as well as the motivation for developing it. Apart from the QH capabilities, the two versions of
¹³⁴ ROMS are nearly identical for the purposes of the work presented here.

¹³⁵ The parent simulation was constructed similarly to the one introduced in Lemarié et al. (2012)
¹³⁶ but with a much finer horizontal resolution. It was used previously in Molemaker et al. (2015). It
¹³⁷ has an orthogonal grid based on a transverse Mercator projection with 1842x962 points, allowing
¹³⁸ a smooth transition of the grid size from 12.5 km at the equator to 8.5 km at high latitudes. The
¹³⁹ south and north extremes of the grid are around 40°S and 55°N, respectively. The simulation is
¹⁴⁰ run for approximately 10.5 years.

¹⁴¹ We used the last 6 years of the parent solution at 5-day intervals to force the open boundary
¹⁴² conditions of the child grid. This grid covers most of the Eastern Equatorial Pacific region, from
¹⁴³ 165°W to 105°W and between ±19°N. Its location was motivated by two criteria: one, the pres-
¹⁴⁴ ence of TIWs at the surface, which flux energy downward in the water column (Ascani et al. 2010);
¹⁴⁵ and two, a smooth bathymetry over a large part of the domain that limits other near-bottom pro-
¹⁴⁶ cesses that can generate turbulence such as lee waves (Figure 1b). The child domain has 1100x700
¹⁴⁷ grid points with a horizontal resolution of 6 km. We ran the child simulation in both the QH and
¹⁴⁸ Hydrostatic (H) mode.

¹⁴⁹ For all simulations, the model bathymetry was interpolated from the Shuttle Radar Topography
¹⁵⁰ Mission (SRTM30_PLUS) dataset based on the 1-min Smith and Sandwell (1997) global dataset,
¹⁵¹ but higher-resolution data was used where available (Becker et al. 2009). The preparation of the
¹⁵² topography in the model was split into two successive steps for each simulation. First, a coars-
¹⁵³ ening procedure with a Gaussian smoothing kernel with a width 8 times that of the topographic
¹⁵⁴ grid spacing was used to ensure that all the grid metrics are smooth at the scale of the resolution.
¹⁵⁵ Second, a so-called log-smoothing procedure was used to ensure that the depth difference between
¹⁵⁶ grid cells normalized by the depth ($\Delta H/H$) did not exceed 0.2. This criteria is based on computa-

¹⁵⁷ tional restrictions for models formulated with a terrain-following coordinate, such as ROMS (see
¹⁵⁸ Beckmann and Haidvogel 1993). To avoid a discontinuity in the grids between the child and parent
¹⁵⁹ simulations, the topography near the boundaries of the nested domain was smoothly matched with
¹⁶⁰ the parent topography over 32 grid points. The maximum depth for the child grid was set to 6000
¹⁶¹ m.

¹⁶² The same climatological datasets were used for forcing the lateral boundaries of the parent sim-
¹⁶³ ulation and the surface forcing for all simulations. At the surface, the wind stress was prepared fol-
¹⁶⁴ lowing a two-step procedure that is described in detail in Lemarié et al. (2012). First, the monthly
¹⁶⁵ climatology of QuikSCAT-based Scatterometer Climatology of Ocean Wind (SCOW; Risien and
¹⁶⁶ Chelton 2008) was adjusted towards the Tropical Atmosphere-Ocean (TAO) buoys data that are
¹⁶⁷ available in the Equatorial Pacific to prevent a recurring bias that can occur in modeled equato-
¹⁶⁸ rial currents with SCOW forcing. Then, daily winds from the CERSAT (French ERS Processing
¹⁶⁹ and Archiving Facility) Mean Wind Fields (MWF) blended product were added to the final wind
¹⁷⁰ stress. We obtained heat fluxes from the Common Ocean-Ice Reference Experiment monthly cli-
¹⁷¹ matology (CORE; Large and Yeager 2009), and incorporated a weak feedback with the modeled
¹⁷² sea surface temperature (SST) (Barnier 1995). Surface evaporation and precipitation were taken
¹⁷³ from the Hamburg Ocean Atmosphere Parameters and Fluxes from Satellite dataset (HOAPS-38;
¹⁷⁴ Andersson et al. 2010) with an additional restoring tendency toward climatological monthly sur-
¹⁷⁵ face salinity from the World Ocean Atlas (WOA; Conkright et al. 2002) to prevent surface salinity
¹⁷⁶ from drifting away from climatological values. Initial and boundary conditions for temperature,
¹⁷⁷ salinity, surface elevation, and the horizontal velocity for the parent domain were taken from the
¹⁷⁸ monthly averaged Simple Ocean Data Assimilation (SODA) ocean climatology (Carton and Giese
¹⁷⁹ 2008).

180 In the vertical, the parent simulation has 50 terrain-following σ -levels that are stretched towards
181 the surface, while the child simulation has 80 vertical levels that are stretched towards both the
182 surface and the bottom. The formulation for the vertical coordinate is described in Shchepetkin
183 and McWilliams (2008) (Eqs. 2.2 and 2.4). In this work, $h_c = 250$ m for both the parent and
184 the child simulations (h_c represents the depth of the transition between flat z -levels and terrain-
185 following σ -levels). The parameter controlling the bottom refinement of the grid is $\theta_b = 1.5$ in the
186 parent simulation and $\theta_b = 4.5$ in the child simulation. At the surface, we used $\theta_s = 6.5$ for both
187 simulations.

188 Since the objective of this paper is to investigate where and when NT effects may occur in the
189 Equatorial Pacific, a free-slip boundary condition was used at the bottom with no bottom drag,
190 allowing us to avoid the generation of high shear through friction. This makes the generation
191 of shear through the critical reflection of ETWs modified by NT effects more distinguishable.
192 However, we have also run simulations with bottom drag in which NT effects are evident. These
193 will be discussed more fully in section 4.

194 Vertical mixing of tracers and momentum was accomplished using the K-profile parameteriza-
195 tion (KPP Large et al. 1994). This parameterization has both boundary layer and interior mixing
196 schemes as described in Large et al. (1994). The interior mixing scheme estimates the mixing
197 coefficients by combining the effects of three mechanisms: shear instability, convective instability
198 and internal wave breaking. Internal wave generated mixing serves to induce a background dif-
199 fusivity, which was set to the default value of 1×10^{-4} m²/s for momentum and 1×10^{-5} m²/s
200 for tracers. The convective component used values of 0.1 m²/s for both diffusivity and viscos-
201 ity for unresolved convective cells when $N^2 < 0$, where N is the Brunt-Väisälä frequency. When
202 $N^2 > 0$, interior diffusivities and viscosities due to shear instability were calculated using a gradi-

203 ent Richardson number formulation as

$$v_s = \begin{cases} v_0 & \text{if } \text{Ri} < 0, \\ v_0[1 - (\text{Ri}/\text{Ri}^c)^2]^3 & \text{if } 0 < \text{Ri} < \text{Ri}^c, \\ 0 & \text{if } \text{Ri}^c < \text{Ri}, \end{cases} \quad (1)$$

204 where $v_0 = 5 \times 10^{-3}$ m²/s was the maximum interior mixing coefficient due to shear instability.

205 Ri is the gradient Richardson number defined as

$$\text{Ri} = N^2 / \left[\left(\frac{\partial u}{\partial z} \right)^2 + \left(\frac{\partial v}{\partial z} \right)^2 \right]. \quad (2)$$

206 The value of the critical gradient Richardson number below which turbulent mixing occurs, Ri^c ,

207 was set to the default value of 0.7, as suggested in Large et al. (1994).

208 Analyses of the abyssal stratification in the parent simulation showed that its values were unre-
209 alistically larger than what has been observed in the equatorial Pacific. DT19 showed that weak
210 stratification of the water column is a crucial criterion for NT effects to be effective, that is, the
211 key non-dimensional parameter controlling the strength of the NT effects is

$$\Gamma = N^2 / \tilde{f}^2. \quad (3)$$

212 When $\Gamma = O(1)$ or smaller, NT effects are important (see DT19). In order to have a realistic strat-
213 ification in the abyss, we modified the stratification profile in the initial and boundary conditions
214 of the child simulation to make it consistent with the observations. To do this, we modified the
215 temperature (T) and salinity (S) fields at each horizontal location following

$$T_{ij}(z_{ij}) = T_{ij}(z_{ij})(1 - \mathcal{M}_{ij}(z_{ij})) + T_{ij}(H_{ij})\mathcal{M}_{ij}(z_{ij}), \quad (4)$$

$$S_{ij}(z_{ij}) = S_{ij}(z_{ij})(1 - \mathcal{M}_{ij}(z_{ij})) + S_{ij}(H_{ij})\mathcal{M}_{ij}(z_{ij}), \quad (5)$$

216 where i and j denote the horizontal indices of the grid in the initial and boundary conditions, z_{ij}
217 denotes the vertical coordinate at location (i, j) , H_{ij} is the depth of the water column at location

218 (i, j) , and \mathcal{M} is a mask that modulates the correction. \mathcal{M} consists of a hyperbolic tangent function
219 that is zero in the upper water column and approaches one smoothly in the abyssal ocean,

$$\mathcal{M}_{ij} = \frac{1}{2} \left(1 - \tanh \left(\frac{z_{ij} - (H_{ij} + h)}{100} \right) \right), \quad (6)$$

220 where h denotes the width of the bottom boundary layer where the stratification is reduced. In the
221 simulations, we set $h = 300$ m based on observed stratification profiles. The first year of simulation
222 for the child runs was used as a spin-up to allow the system to adjust to these modifications, and
223 we used the remaining 5 years of simulation for the analyses presented in the next sections. An
224 example of the stratification profile in both the parent and child simulations at 110°W between
225 $\pm 2^{\circ}\text{N}$, along with profiles from observations, illustrates that N^2 in the child simulation reaches
226 values that are closer to \tilde{f}^2 at this location compared to the parent simulation, more in line with
227 the observations (Figure 2).

228 3. Results

229 a. Equatorial dynamics

230 A comprehensive model validation of the circulation is beyond the scope of this paper, which is
231 devoted to the NT effects. Lemarié et al. (2012) has already conducted a detailed validation of a
232 simulation similar to the parent simulation that we used for this work (our parent simulation has
233 a higher spatial resolution than the one from Lemarié et al. 2012, but it uses the same numerical
234 algorithms, bathymetry, surface forcing and boundary conditions). They showed that the model
235 reproduces the key features of the observed circulation in the Equatorial Pacific. In this section,
236 we instead focus on the extent to which NT effects have an effect on the properties of the Equa-
237 torial Pacific that are the most relevant to the problem at hand, namely the structure of the mean
238 circulation and the ETW field.

239 1) MEAN CIRCULATION

240 We contrast the mean zonal currents averaged over 120-160°W in the H and QH simulation (Figure
241 3). The mean equatorial current system is composed of the eastward flowing North Equatorial
242 Counter-Current, the Equatorial Undercurrent, the South and North Subsurface Counter-Current,
243 the westward flowing South and North Equatorial Currents and the Equatorial Intermediate Cur-
244 rent. All of these currents are found in both the H and QH simulations with similar spatial struc-
245 tures and amplitudes, and are consistent with observations (see Cravatte et al. 2017, for a similar
246 calculation from the Argo float dataset). The low-latitude subsurface counter-currents highlighted
247 in Méneguen et al. (2019) are also visible in both simulations on each side of the equator.

248 2) EQUATORIAL WAVE FIELD

249 Farrar (2008) derived the wavenumber-frequency power spectrum of sea surface height from
250 altimetry data between 7°S-7°N to examine the dispersion relation of wavelike variability with
251 periods of about 20 to 200 days in the equatorial Pacific Ocean (see his Figure 2). Following up on
252 these results, Farrar and Durland (2012) used the surface dynamic height relative to 500 dbar from
253 the TAO/TRITON moorings between 5°S-5°N to derive a wavenumber-frequency power spec-
254 trum focusing on wavelike variability with periods of about 3 to 15 days in the equatorial Pacific
255 Ocean (see their Figure 5). These two studies provided a quantification of the full ETW spectrum
256 from observations in the equatorial Pacific Ocean. Using a similar approach, we calculated the
257 wavenumber-frequency power spectrum of the surface meridional velocity field averaged over a
258 range of latitudes and longitudes corresponding to the limits of the domain of the child simulations
259 (Figure 4). In the equatorial regions, meridional velocities are a good proxy for ETWs since the
260 zonal velocity is dominated by the strong zonal flows. However, using the meridional velocity
261 inherently removes the Kelvin wave part of the spectrum from our analysis. Given our model's

262 spatial and temporal resolution, we were able to resolve wavelike variability with periods from
263 two days to a year, and zonal wavelengths exceeding 20 km.

264 The power spectral density of the meridional velocity in the H simulation is very similar to that
265 in the QH simulation. It has spectral peaks that lie at similar locations on the analytical dispersion
266 curves of the first and second baroclinic modes in a resting ocean (white lines in Figure 3), showing
267 that NT effects do not affect the dispersion of the waves as described in DT19. In addition, the
268 spectral amplitude of each wave is also very similar between the H and QH simulations. Note
269 that because of the Doppler shift induced by the mean zonal currents on the waves, some maxima
270 in the power spectrum may lie close to but not entirely on the theoretical curves (McPhaden and
271 Knox 1979).

272 Overall, the model's spectra have similar spectral peaks as the ones calculated by Farrar (2008)
273 and Farrar and Durland (2012) from observations (excluding the Kelvin wave part of the spectrum).

274 The highest peak occurs near 33 days and is associated with the first baroclinic mode Rossby wave.
275 The second largest peak occurs near 17 days and is associated with the westward-propagating
276 Yanai wave. Both of these waves have also been seen in subsurface observations (Lyman et al.
277 2007), and are thought to be triggered by the TIWs that are clearly visible in the Sea Surface
278 Temperature field in Figure 1. At lower frequencies, there is significant energy around 60 days
279 that corresponds to the second baroclinic mode Rossby wave. The Yanai wave dispersion curves
280 for the first and second baroclinic modes have other peaks at 23, 14 and 10 days that have also
281 been reported in observations (Farrar and Durland 2012; Shinoda 2012). At higher frequencies,
282 we see many elevated spectral peaks at low zonal wavenumbers. The peak around 6 days has also
283 been found by Farrar and Durland (2012), who associated it to the second baroclinic mode of an
284 eastward-propagating IGW. The elevated signal around 5 days was observed by Wunsch and Gill
285 (1976), and is associated with the variability of the meridional winds. According to Farrar and

286 Durland (2012), it would correspond to a double resonance of both the first baroclinic mode, first
287 meridional mode IGW and the second baroclinic mode, second meridional mode IGW.

288 The model allows us to investigate the ETW spectrum near the bottom as well. Using the same
289 approach as in the previous paragraph, we calculated the wavenumber-frequency power spectrum
290 of the meridional velocity field averaged over the bottom σ -layer in the child simulations. The
291 results are shown in Figure 5 for the H simulation but, as with the surface calculation, they are
292 qualitatively similar to those from the QH run. Spectral peaks similar to the surface peaks were
293 found, suggesting that most waves propagate from the surface to the bottom in our simulations.

294 Note that the energy content of the waves at the bottom is lower than that at the surface. This
295 decrease in energy is expected since, under realistic stratification, the magnitude of the horizontal
296 velocity eigenfunction for the first baroclinic mode is much greater at the surface than it is at the
297 bottom for all waves (this is also true to a lesser extent for the second baroclinic mode). Dissipation
298 of energy as the waves are propagating down in the water column might also be at play. In addition,
299 the relative magnitude of each peak is different, suggesting that some waves have either been
300 damped more than others as they propagate down, or that some waves have left or entered the
301 domain of the simulation through the lateral boundaries at depth. For example, the 17-day Yanai
302 wave is weaker than the 20-day Yanai wave in the abyss but stronger at the surface. Rossby
303 and Yanai waves with relatively large zonal wavenumbers are present in the bottom spectrum yet
304 absent near the surface. This enhancement of energy at shorter scales might be due to the presence
305 of the bottom topography, which can lead to scattering and thus generate higher wavenumbers.

306 Overall, these results show that our simulations reproduce well the ETW field seen in the obser-
307 vations. In addition, these waves propagate down into the deep ocean, hence providing a realistic
308 forcing mechanism for assessing the presence or lack thereof of critical reflection induced by NT
309 effects, as predicted by DT19.

310 b. Abyssal mixing

311 We also contrasted the turbulent diffusivity in the H and QH simulations averaged over the
312 bottom 1000 m of the water column and over the five years of simulation (Figure 6).

313 In the H case, the diffusivity is enhanced between $\pm 2^\circ$ where the currents are the strongest and in
314 areas of rough topography. The diffusivities are particularly large in the western part of the domain
315 because of the presence of rough topography (see Figure 1b). In the QH case, however, elevated
316 diffusivities are also found outside of the $\pm 2^\circ$ equatorial band, with enhanced values extending
317 from 8°S to 14°N . Most of the high diffusivity values are found between 120°W and 155°W in the
318 QH run. In the eastern part of the domain, the QH and H simulations look very similar.

319 Locations with higher diffusivities are associated with enhanced bottom shear in the simulations
320 (Figure 7). While most of the vertical shear is confined to $\pm 2^\circ$ or over rough topography in the H
321 case, large values of the shear are seen over smooth topography and outside the equatorial band in
322 the QH case. In some of these areas, the vertical shear in the QH simulation is more than 100 times
323 greater than that in the H simulation. The locations of enhanced shear and subsequent mixing in
324 the QH run match notably areas where $\Gamma \leq 1$ (shown within the contour line in Figures 6 and 7),
325 consistent with the theory described in DT19.

326 To highlight the vertical extent of the mixing (Figure 8) and the corresponding shear (Figure
327 9), we focus on a section along the 130°W longitude line. The diffusivities are enhanced in a
328 bottom boundary layer in the QH case comparable to the surface boundary layer, and extend for
329 up to 300 m off the bottom. This bottom boundary layer is completely absent in the H simulation.
330 Enhanced diffusivities are also found higher in the water column in the $\pm 2^\circ$ equatorial band but
331 this is the case for both the H and QH simulations. As highlighted in Figure 9, the diffusivities
332 near the bottom in the QH case are associated with higher vertical shear. In the H case, the shear

333 is confined to the surface and in the $\pm 2^\circ$ equatorial band in the abyss. The ratio of the shear in
334 the QH and H simulations (bottom panel) shows more clearly the vertical extent of the enhanced
335 shear in the QH simulation. Overall, enhanced values in the QH case can reach up to 1000 m off
336 the bottom.

337 To understand better the properties of the shear that is generated in the QH simulation, we
338 have calculated the frequency spectrum of the vertical shear in the bottom 500 m of the water
339 column as a function of latitude at 130°W (Figure 10). In the H simulation, there is enhanced
340 energy at only low frequencies and close to the equator, whereas in the QH simulation, enhanced
341 energy is seen at all latitudes. In the latter case, the spectrum peaks around the inertial frequency,
342 showing that the shear that is generated in the QH simulation is near-inertial. Within the near-
343 inertial band, some frequencies are more energetic than others and correspond to specific inertial
344 latitudes. These frequencies correspond to the frequencies of particular ETWs that we found in the
345 deep in our simulations (see Figure 5), suggesting that the ETWs are responsible for the enhanced
346 mixing in the QH run. A major peak, for example, occurs at a frequency of around 0.19 day^{-1}
347 and corresponds to an IGW with an inertial latitude of 5.5° . In addition, it can be seen that the
348 enhanced energy in the H run is mostly super-inertial whereas it extends a bit in the sub-inertial
349 region in the QH case, consistent with the sub-inertial propagation of IGWs allowed when the NT
350 effects are active.

351 To better visualize the spatial and temporal variability of the shear, Hovmöller diagrams of the
352 vertical shear of the meridional velocity as a function of latitude at 130°W are shown in Figure 11.
353 In the QH case, shear outside of the $\pm 2^\circ$ equatorial band forms stacked bands that oscillate near
354 the local inertial frequency. The shear bands have a non-zero meridional wavenumber, with an
355 equatorward phase velocity. However, the wave beams that are associated with these shear bands
356 propagate poleward, away from their generation location. We highlight the vertical structure of

357 the shear on the 5.5°S line (which corresponds to the inertial latitude of the 5-day wave) in Figure
358 12. In particular, there is one high-shear event occurring between Dec 15 and January 15 with a
359 downward phase propagation.

360 **4. Discussion**

361 In the previous section, we showed the diffusivities in the abyss were enhanced in a large part
362 of the domain in the QH simulation compared to that in the H simulation. We further showed that
363 the enhanced diffusivities were associated with inertial vertical shear that develops when $\tilde{f} \neq 0$.
364 Our hypothesis is that the vertical shear is generated through the mechanism of critical reflection
365 when ETWs reflect off the bottom, as predicted by DT19's theory.

366 It is possible to understand the theory better by looking at the governing equation for inviscid,
367 zonally-invariant, linear IGWs over an f -plane,

$$(N^2 + \tilde{f}^2)\psi_{yy} + 2\tilde{f}f\psi_{yz} + (f^2 - \omega^2)\psi_{zz} = 0, \quad (7)$$

368 where ω is the frequency of the wave, and ψ is the streamfunction (i.e., $v = \partial\psi/\partial z$ and $w =$
369 $-\partial\psi/\partial y$).

370 Equation (7) admits wavelike solutions where it is hyperbolic, i.e., where $B^2 - AC > 0$ with
371 $A = N^2 + \tilde{f}^2$, $B = \tilde{f}f$ and $C = f^2 - \omega^2$. This constraint gives a lower bound for the frequency of
372 the wave:

$$\omega_{min} = |f| \sqrt{1 - \frac{\tilde{f}^2}{N^2 + \tilde{f}^2}} = |f| \sqrt{\frac{\Gamma}{1 + \Gamma}}. \quad (8)$$

373 Note that, when $\tilde{f} = 0$, we found the usual lower bound for IGWs under the traditional approxi-
374 mation: $\omega_{min} = |f|$. With $\tilde{f} \neq 0$ and $\Gamma \leq 1$, values of ω that are significantly lower than $|f|$ are
375 possible.

³⁷⁶ The characteristic curves of (7) represent rays along which wave energy propagates. The slope
³⁷⁷ of these rays is equal to

$$\mu^\pm = \frac{B \pm \sqrt{B^2 - AC}}{A}. \quad (9)$$

³⁷⁸ To get the direction of energy propagation, we derive a dispersion relation using a plane wave
³⁷⁹ solution $\psi(y, z) \sim e^{i(ly + mz)}$ in (7):

$$\omega^2 = f^2 + 2\tilde{f}f \frac{l}{m} + (N^2 + \tilde{f}^2) \frac{l^2}{m^2}. \quad (10)$$

³⁸⁰ This is the dispersion relation for 2D inertia-gravity waves over a NT f -plane. Note that $\mu^\pm =$
³⁸¹ $-\frac{l}{m}$.

³⁸² Taking the gradient of (10) with respect to the wave vector yields the group velocity of the wave:

$$(c_g^y, c_g^z) = \frac{l(N^2 + \tilde{f}^2) + mff\tilde{f}}{m^2\omega} \left(1, -\frac{l}{m}\right), \quad (11)$$

³⁸³ which gives the direction and speed of energy propagation, and constrains the characteristics along
³⁸⁴ which the incoming and reflected waves propagate.

³⁸⁵ At the inertial latitude, $\mu_{\omega=f}^\pm = 0$ when $\tilde{f} = 0$. However, $\mu_{\omega=f}^+ = \frac{2f}{\tilde{f}}(1 + \Gamma)^{-1}$ in the NT case
³⁸⁶ when $\tilde{f} \neq 0$. If Γ is low enough, $\mu_{\omega=f}^+$ is significant, allowing for vertical propagation of energy at
³⁸⁷ the inertial latitude along the steep characteristic. Since $\mu_{\omega=f}^- = 0$, the second characteristic is flat
³⁸⁸ and therefore ray tubes becomes compressed to an infinitesimally small layer when reflecting off
³⁸⁹ a flat bottom, resulting in critical reflection. This mechanism is illustrated in Figure 13. It requires
³⁹⁰ three key elements to occur: a downward flux of ETW energy along the steep characteristic, $\Gamma \leq 1$
³⁹¹ such that $\mu_{\omega=f}^+$ is significant, and a bottom slope low enough such that ray tubes are compressed
³⁹² enough to amplify the reflected wave.

³⁹³ In the next subsections, we discuss whether the conditions are met for critical reflection to occur.
³⁹⁴ Then, we look at the properties of the shear that develops in the QH simulation to examine whether

395 our hypothesis is consistent with the mechanism of critical reflection described above. Finally, we
396 discuss the implications of the enhanced diffusivities for the abyssal stratification and diapycnal
397 upwelling.

398 *a. Vertical propagation of equatorial waves*

399 To investigate whether ETWs can flux energy on the steep characteristics near the bottom where
400 enhanced vertical shear is found, we selected six spectral peaks from Figures 4 and 5 to track their
401 vertical propagation of energy: the 33-day Rossby wave, the 23-day Yanai wave, the 17-day Yanai
402 wave, the 6-day IGW, the 5-day IGW and the 3-day IGW.

403 The location where these waves are generated at the surface can be identified by calculating the
404 variance of the meridional velocity filtered around the frequency for each of the six waves (Figure
405 14). Depending on the type of wave, maxima in the variance are found in different locations. The
406 3-day IGW is mostly generated near 125–140°W to the north of the Equator, while the 5-day IGW
407 has a peak around 130–145°W on the south side of the Equator. The 6-day IGW is more spread
408 out, with a stronger signal on the southern side of the equator between 110°W and 150°W. Both
409 Yanai waves have peaks centered at the equator in the eastern side of our domain, between 110°W
410 and 130°W. The 33-day Rossby wave is mostly generated in the northern hemisphere, between
411 120–140°W.

412 In Figures 4 and 5, we have shown that the six waves considered here lie on the theoretical
413 dispersion curves for baroclinic modes 1 and 2. The dispersion relation for such waves was derived
414 by Cox (1980):

$$c = \frac{-\beta(2n+1) \pm \sqrt{\beta^2(2n+1)^2 + 4(k^2 + \beta k \omega^{-1})\omega^2}}{2(k^2 + \beta k \omega^{-1})}, \quad (12)$$

415 where c denotes the phase speed for the n^{th} baroclinic mode Kelvin wave, k and ω are respectively
 416 the zonal wavenumber and frequency of the wave, and $\beta = 2\Omega/R_E$ is the meridional gradient of
 417 the vertical component of the Coriolis parameter at the equator (Ω is the Earth's angular veloc-
 418 ity and R_E is the Earth's radius). The effects of variable stratification are manifest in the local
 419 wavenumber,

$$m(z) = N(z)/c. \quad (13)$$

420 From equations (12) and (13), it is possible to derive the expressions for the zonal group velocity,
 421 c_g^x , and the vertical group velocity, c_g^z :

$$c_g^x = \frac{c^2(2k + \beta\omega^{-1})}{2\omega + \beta kc^2\omega^{-2}}, \quad (14)$$

$$c_g^z = -\frac{\omega^2 + \beta kc^2\omega^{-1} + k^2 c^2}{N(2\omega c^{-1} + \beta kc\omega^{-2})}. \quad (15)$$

422 We used equations (14) and (15) to quantify the pathways of propagation for the six waves
 423 we have considered. For each wave, we randomly generated a range of frequencies and zonal
 424 wavenumbers that are appropriate for the wave of interest. We used the map of the variance of the
 425 meridional velocity at the surface for each wave (Figure 14) to construct a probability distribution
 426 for the starting point of the rays, with higher probabilities in regions where the variance is larger.
 427 We used the stratification profile measured by Holmes et al. (2016) in the Eastern Pacific Equatorial
 428 and shown in Figure 2 to trace the rays.

429 For each wave, we launched 20 rays (Figure 15). Our results show that the Rossby and IGW
 430 rays are nearly vertical while the Yanai waves propagate away from their generation longitude to
 431 the east. In our calculation, most of the IGW and Rossby wave rays reach the bottom between
 432 125–145°W, which is the area where we see the largest diffusivities in the QH run. The IGWs are
 433 in particular confined to this longitude band, which potentially explains the enhanced diffusivities
 434 that develop at higher latitudes since their inertial latitudes lie further away from the equator. The

435 Yanai waves propagate eastward, and most of them reach the seafloor out of our domain. Note
436 that depending on the type of wave, the travel time from the surface to the bottom varies greatly:
437 while the IGW reach the seafloor within a few days, it can take several months for the Yanai and
438 Rossby waves to hit the bottom.

439 *b. Bottom slope and the slope of the steep characteristic*

440 The two other key ingredients needed for critical reflection are linked to the slope of the seafloor
441 and the slope of the steep characteristic at the inertial latitude of the wave, $\mu_{\omega=f}^+$.

442 If the steep characteristic has a slope that is too low, the compression of ray tubes will be limited,
443 weakening amplification by the critical reflection mechanism. Similarly, if the slope of the seafloor
444 is too high, the compression of ray tubes upon reflection is reduced and the critical reflection
445 mechanism is not as effective. Therefore, a key metric for the effectiveness of the critical reflection
446 mechanism is the ratio of $\mu_{\omega=f}^+$ to the slope of the seafloor, which we plot in Figure 16. Over most
447 of the domain, the ratio is large, suggesting that the mechanism of critical reflection is efficient
448 there. The ratio is small over rough topography as expected. However, it is also small at the
449 equator. To understand why, consider the limit when $\Gamma \ll 1$, which is the case in most parts of the
450 domain at the bottom. In this limit, the slope of the steep characteristics becomes $\mu_{\omega=f}^+ = 2f/\tilde{f}$.

451 Close to the equator, this expression is approximately to $\mu_{\omega=f}^+ \approx 2\phi$, where ϕ is the latitude.
452 Therefore, close to the equator, the mechanism of critical reflection is expected to be less effective
453 than away from the equator. This was observed in the idealized simulations of DT19 where it was
454 seen that the longer the period of the ETW and hence the lower the inertial latitude, the weaker the
455 critical reflection. We appear to see this effect in our realistic simulations as well. For example,
456 the ratio of the vertical shear squared in the QH to the H simulation increases with latitude (Figure
457 7). In addition, we see that the higher frequency ETW result in stronger shears. For example, the

458 most visible beams of shear seen in Figure 11 originate from 5.5° and 8° , which correspond to the
459 inertial latitudes of the 3-day and 5-day IGW that we see at the surface and at the bottom in our
460 simulations (Figures 4 and 5).

461 We should note, however, that beyond a certain latitude (around 10° in the northern hemisphere
462 and 8° in the southern hemisphere), the ratio of the vertical shear decreases again. It also exhibits
463 an asymmetry in the east-west direction, suggesting that factors other than latitude come into play.
464 In particular, $\mu_{\omega=f}^+$ depends on Γ which is a function of both the stratification and \tilde{f} . While \tilde{f}
465 decreases with latitudes, the abyssal stratification can vary laterally. These two factors can lead
466 to areas where $\Gamma > 1$ at the bottom. We highlight these regions in Figures 6 and 7, where they
467 are delineated with the $\Gamma = 1$ contour. As predicted by the theory, the enhanced vertical shear and
468 mixing occur over areas where $\Gamma < 1$. In the southern hemisphere, this area extends down to 10°S .
469 In the northern hemisphere however, Γ remains below one past 10°N . In the simulation featured in
470 this paper, the domain is not big enough to determine the meridional limit where $\Gamma \leq 1$. However,
471 we have run a lower-resolution simulation that extends to $\pm 20^\circ\text{N}$ and that suggests that values of
472 $\Gamma < 1$ are found up to 18°N in the Eastern Equatorial Pacific.

473 *c. Properties of the vertical shear*

474 The analyses described above suggest that the key elements needed for critical reflection are met
475 in the QH run and coincide with the areas where shear is enhanced. To rigorously associate the
476 enhanced shear with DT19's theory, however, we still need to demonstrate that the properties of
477 the shear that develops in our simulation are consistent with the ones predicted by DT19.

478 First, as shown in Figure 10, the vertical shears in the QH simulation with the most energy have
479 near-inertial frequencies. This is consistent with DT19's theory since critical reflection preferen-
480 tially amplifies shear at the inertial latitude. As evident in Figure 11, these inertial waves have

a non-zero horizontal wavenumber. Although this is not permitted for traditional IGWs, it is allowed when $\tilde{f} \neq 0$. From (10), $\omega = f$ when $l = 0$, or when $\frac{l}{m} = -\frac{2f\tilde{f}}{N^2 + \tilde{f}^2}$, which yields a meridional wavelength, $\lambda_y = \lambda_z \frac{N^2 + \tilde{f}^2}{2|f|\tilde{f}}$, where λ_z is the vertical wavelength of the wave. From Figure 12, we observe that for the first beam $\lambda_z = 500\text{m}$. Using the value of the stratification, $|f|$ and \tilde{f} at the latitude of the beam, the factor $(N^2 + \tilde{f}^2)/2|f|\tilde{f}$ is equal to $\sim 4 \times 10^2$, which would yield a meridional wavelength of $\lambda_y \sim 20\text{ km}$ ($\sim 0.2^\circ$). This value is similar to the lateral wavelength of the beam seen in Figure 11.

Apart from oscillating at frequencies near f , the shear has a very particular phase propagation. As illustrated in Figure 11, near 5°S for example, phase propagates equatorward while energy propagates poleward (i.e., the direction of beam propagation). This apparent opposition of the phase and group velocity in the meridional direction is consistent with the theory for IGWs when NT effects are taken into account.

A schematic of the wave characteristics with their corresponding group and phase velocity vectors for $\tilde{f} \neq 0$ in the superinertial ($\omega > f$), inertial ($\omega = f$) and subinertial limits ($\omega < f$) illustrates this point (Figure 17). Note that this schematic is for IGWs in the northern hemisphere. We first focus on the subinertial limit since the beams propagate poleward of their inertial latitude and hence become subinertial, which is allowed when NT effects are taken into account. The behavior of these waves is very different than IGWs under the traditional approximation, that is the phase and group velocity take the same sign in the vertical and the opposite sign in the meridional on the shallow characteristic (their behavior on the steep characteristic is similar to that of traditional IGWs). As described in DT19 (see their Figure 5), after critical reflection, IGWs propagate away from the inertial latitude poleward and upward along the shallow characteristic (blue line). Once the wave reaches the separatrix where the wave equation transitions from hyperbolic to elliptic, it reflects back down on the steep characteristic until it reaches the seafloor and reflects back up on

505 the shallow characteristic, and so on. Therefore, while the direction of energy propagation changes
506 every time the wave switches from one characteristic to the other, the meridional phase propaga-
507 tion always points toward the equator. In the superinertial regime, the reflected wave propagates
508 upward and equatorward along the shallow characteristic. In this case, we have also an equator-
509 ward phase propagation, potentially explaining why all the beams that we see in Figure 11 have
510 an equatorward phase propagation.

511 Note also that the vertical phase propagation of the first beam event in Figure 12 is downward.
512 We can see (Figure 11) that the latitude chosen to plot the vertical section in Figure 12 is slightly
513 equatorward of the first beam event. Therefore, we are at the border of the superinertial regime for
514 this beam event. In the superinertial regime, where the reflected wave propagates upward along
515 the shallow characteristic, the phase propagation is downward (Figure 17), consistent with what
516 we see in the simulation.

517 *d. Implication for abyssal stratification and upwelling*

518 The enhanced diffusivities in the abyss associated with NT effects have two main consequences:
519 weakening the stratification and driving diapycnal motions. To quantify the differences in strati-
520 fication cause by NT effects, we calculated histograms of the buoyancy frequency in the bottom
521 1000 m of the water column and contrasted the distributions in the H and QH runs (Figure 18).
522 The histograms have been calculated across the entire domain. We can see that while the mean
523 and median values of the distributions are similar in the H and QH runs, the 10th percentile is
524 much lower in the QH case (about two order of magnitude lower in some regions), suggesting
525 that NT effects act to skew the distribution towards low values in areas where there are enhanced
526 diffusivities.

527 To assess the impact that the enhanced diffusivities that develop in the abyss may have on the
528 diapycnal transport of water masses, we calculate the diabatic vertical velocity, defined as

$$w_{dia} = \left(\frac{\partial \kappa}{\partial z} N^2 + \kappa \frac{\partial N^2}{\partial z} \right) / N^2. \quad (16)$$

529 Histograms of the diapycnal vertical velocity in the bottom 1000 m of the water column for the
530 H and QH runs are contrasted in Figure 19. It can be seen that while most values are near-zero in
531 the H case (except near the equator where there is a nearly symmetric distribution of positive and
532 negative diapycnal velocities), the distribution is skewed towards positive values in the QH case in
533 areas where there is enhanced mixing. This effect is more clear when looking at the mean of the
534 distribution, which is very close to zero in the H run except right at the equator where it is slightly
535 positive, while it is skewed to positive values in the QH run in areas where enhanced diffusivities
536 have been found. While the diffusivities are bottom-intensified, they induce diapycnal upwelling
537 not downwelling because the stratification increases with height off the bottom (e.g., Figure 2) and
538 the second term in (16) dominates over the first.

539 We have integrated the diapycnal vertical velocity across the entire numerical domain of the
540 child grid to calculate a vertical volume transport quantity, Ψ_{dia} , as

$$\Psi_{dia} = \int \int w_{dia} dx dy, \quad (17)$$

541 which is expressed in units of Sverdrups (Sv). We found $\Psi_{dia}^H = 2.5$ Sv and $\Psi_{dia}^{QH} = 23$ Sv, sug-
542 gesting that the process could contribute substantially to the AMOC.

543 *e. Impact of the bottom drag*

544 To investigate whether our results hold in the presence of bottom drag, we have run the same H
545 and QH simulations as before except that we allowed for bottom stress which was parameterized
546 using a quadratic drag law. Bottom drag enhances the vertical shear, making it more difficult to

547 distinguish the shear generated by critical reflection. However there is a distinguishable difference
548 in diffusivities between the QH and H simulations even in the presence of drag. We illustrate
549 this using the turbulent diffusivity averaged over the bottom 1000 m of the water column, over all
550 longitudes, and over the 5 years of simulation (Figure 20). It can be seen that the enhancement
551 in diffusivities in the QH simulations relative to the H simulations is similar with or without drag,
552 showing that NT effects are evident even when bottom drag is active.

553 5. Conclusions

554 By contrasting realistic numerical simulations of the Eastern Equatorial Pacific ocean run with
555 the hydrostatic and quasi-hydrostatic approximations and theory, we have shown that NT effects
556 modify the dynamics of ETWs in the deep. In the weakly-stratified abyss, the reflection of ETWs
557 off the bottom are modified by the NT effects, and the waves undergo critical reflection at their
558 inertial latitude. As a consequence, strong inertial vertical shear is generated and drives mixing
559 that is enhanced primarily between 120–150°W and 8°S–14°N.

560 There are still some questions that remain to be answered. In particular, the presence of enhanced
561 shear and subsequent mixing at relatively high latitudes (between 3–8°S and 3–14°N) suggests
562 that IGW with higher frequencies are found near the bottom in these areas. Whether these waves
563 are generated by surface forcing or correspond to higher harmonics of the dominant ETWs formed
564 by nonlinear wave-wave interactions as was seen by DT19 remains to be investigated.

565 Overall, these results show that NT effects could contribute significantly to the diapycnal up-
566 welling of the abyssal equatorial circulation inferred by inverse models. Our study is however
567 limited by the Richardson-number dependent mixing scheme that we used, which parametrizes
568 the strength of the turbulent diffusivity. Further work will focus on using turbulence resolving
569 simulations to study mixing driven by critical reflection and to parameterize its effects. In addi-

570 tion, because the shape of the stratification profile in the abyss is crucial for the resulting upwelling,
571 it is also necessary to investigate whether the feature shown in Figure 2 is ubiquitous in the oceans.
572 It would also be interesting to extend these results to other equatorial basins and provide a quan-
573 titative estimate of the potential contribution of the NT effects to closing deep cell of the MOC
574 globally.

575 Finally, we hope that these results will motivate further observational studies in the abyssal equa-
576 torial ocean. To our knowledge, the only full-depth cross-equatorial microstructure profiles that
577 have been made in the Eastern Equatorial Pacific were documented in Holmes et al. (2016), which
578 are a main motivation for this study. We have investigated other microstructure profiles available
579 in the Microstructure Database (<https://microstructure.ucsd.edu/>). Unfortunately, none
580 of the profiles available in this database can be used to test the findings from this paper since the
581 only profiles that were made over the full depth of the water column are either too far from the
582 equator (i.e., more than 20° away from the equator) or were obtained over rough topography. The
583 only exception are the observations made in the Atlantic between 10° – 25°S during the Brazil
584 Basin Tracer Release Experiment. These results are described in Polzin et al. (1997) and point to
585 weak mixing rates over smooth topography. We have estimated the abyssal stratification from the
586 data obtained during this experiment and found that its values are much higher than the ones mea-
587 sured by Holmes et al. (2016) in the Eastern Pacific, making $\Gamma >> 1$ at the bottom of the ocean,
588 which would imply that mixing due to NT effects would not be expected in this region. In addition,
589 the equatorial wave field is weaker in the Atlantic versus the Pacific (Ascani et al. 2010). These
590 facts all point to the Pacific being favored over the Atlantic for diapycnal upwelling in the deep
591 branch of the MOC associated with NT effects. This hypothesis is consistent with the findings of
592 Lumpkin and Speer (2007), that most of the abyssal return flow that closes the AMOC is occur-
593 ring in the Pacific ocean. Clearly, more observational efforts are needed to evaluate the mechanism

described here in the abyssal equatorial ocean and the Eastern Pacific is the most relevant area of study for that.

Acknowledgments. This work was a collaborative effort between scientists from France and the United States facilitated by a grant and a fellowship from the France-Stanford Center for Interdisciplinary Studies. It has also received support from a consortium of French research agencies, as part of CROCO’s development project (GdR CROCO). Jonathan Gula was funded by the French National Agency for Research (ANR-19-CE01-0002-01). Jeroen Molemaker was funded by the Office of Naval Research (N00014-08-1-0597). B. Delorme gratefully acknowledges the hospitality of researchers, students and staff at the Laboratoire d’Études en Géophysique et Océanographie Spatiales (LEGOS) and at the Laboratoire d’Océanographie Physique et Spatiale (LOPS) for hosting him over the course of this research project and making his stay very enjoyable and intellectually rewarding. Finally, we would like to acknowledge the two reviewers for their comments; we are particularly grateful to T. Durland for clarifying some subtleties of the spectral analysis of equatorial waves.

APPENDIX

Quasi-Hydrostatic version of CROCO (CROCO_QH)

By default, CROCO solves the free-surface primitive equations using a robust and efficient time-splitting implementation (Shchepetkin and McWilliams 2005; Debreu et al. 2012). The primitive equations can be extended to form the quasi-hydrostatic (QH) equations, relaxing the hypothesis of weak horizontal Coriolis force (White and Bromley 1995; Marshall et al. 1997), thus adding a non-hydrostatic pressure component that is solved diagnostically.

615 In geophysical fluid dynamics, the traditional approximation (TA) takes the Coriolis force only
 616 partially into account by neglecting its components proportional to the cosine of latitude: $\tilde{f} =$
 617 $2\Omega \cos\varphi$ (see Gerkema et al. 2008, for a review). The justification for the TA lies in the hypothesis
 618 that the depth of the oceans is very thin compared to the radius of the Earth. The vertical motions
 619 must then be much weaker than the horizontal ones, rendering the non-traditional (NT) Coriolis
 620 terms (i.e., associated with \tilde{f}) insignificant compared to the traditional terms (i.e., associated with
 621 f) and rendering the pressure field nearly hydrostatic. Similarly, strong vertical stratification in
 622 density, which suppresses vertical motions, also diminishes the role of NT terms. However, as
 623 shown in Delorme and Thomas (2019), this argument becomes weak near the equator since $\tilde{f} >>$
 624 f , or in areas where the stratification is weak. In addition, the QH momentum equations are shown
 625 to be more dynamically consistent than the primitive hydrostatic equations and to correctly imply
 626 conservation laws for energy, angular momentum, and potential vorticity (White and Bromley
 627 1995).

628 A1. Equations in Cartesian coordinate

629 The momentum balance in the zonal and meridional directions (x, y) is extended to include \tilde{f}
 630 terms (zonal u component):

$$\frac{\partial u}{\partial t} = -\vec{\nabla} \cdot (u\vec{v}) + fv - \widetilde{\tilde{f}w} - \frac{\partial \phi}{\partial x} + \mathcal{F}_u + \mathcal{D}_u \quad (\text{A1})$$

$$\frac{\partial v}{\partial t} = -\vec{\nabla} \cdot (v\vec{v}) - fu - \frac{\partial \phi}{\partial y} + \mathcal{F}_v + \mathcal{D}_v \quad (\text{A2})$$

631 The QH balance is used for the vertical momentum equation, where the zonal flow partially
 632 balances the pressure gradient:

$$\frac{\partial \phi}{\partial z} = -\frac{\rho g}{\rho_0} + \widetilde{\tilde{f}u} \quad (\text{A3})$$

633 The variables used are :

634 • $\mathcal{D}_u, \mathcal{D}_v$: diffusive terms

635 • $\mathcal{F}_u, \mathcal{F}_v$: forcing terms

636 • $f(x, y)$: Traditional Coriolis parameter $2\Omega \sin \varphi$

637 • $\tilde{f}(x, y)$: Non-traditional Coriolis parameter $2\Omega \cos \varphi$

638 • g : acceleration of gravity

639 • $\phi(x, y, z, t)$: dynamic pressure $\phi = P/\rho_0$, with P the total pressure

640 • $\rho_0 + \rho(x, y, z, t)$: total in-situ density

641 • u, v, w : the (x, y, z) components of vector velocity \vec{v}

642 **A2. CROCO_QH Implementation**

643 CROCO is implemented in a generalized stretched vertical coordinate system and orthogonal
644 coordinate transformation in the horizontal that allows laterally variable grid resolution and orien-
645 tation. In this case, NT terms for both horizontal momentum components are needed:

$$NT_x = -\tilde{f}w \cos \alpha \quad (\text{A4})$$

$$NT_y = +\tilde{f}w \sin \alpha \quad (\text{A5})$$

646 where α is the angle between North and y grid axis. The non-traditional term $NT_z = \tilde{f}u$ in the
647 quasi-hydrostatic equation is introduced as a correction to density:

$$\frac{\partial \phi}{\partial z} = -\frac{(\rho + \delta\rho)}{\rho_0} g \quad (\text{A6})$$

648 with

$$\delta\rho = -\frac{\rho_0}{g} \tilde{f}(u \cos \alpha - v \sin \alpha) \quad (\text{A7})$$

649 CROCO_QH has been validated on standard QH test cases using the full non-hydrostatic equa-
650 tions that had similar solutions. Obviously, the QH version is much faster than the fully non-
651 hydrostatic model and, therefore, a better choice for our problem.

652 **References**

- 653 Andersson, A., K. Fennig, C. Klepp, S. Bakan, H. Grassl, and J. Schulz, 2010: The Hamburg
654 Ocean Atmosphere Parameters and Geography Fluxes from Satellite Data – HOAPS-3. *Earth*
655 *Syst. Sci. Data*, **2**, 215–234, doi:10.5194/essd-2-215-2010.
- 656 Ascani, F., E. Firing, P. Dutrieux, J. P. McCreary, and A. Ishida, 2010: Deep Equatorial Ocean
657 Circulation Induced by a Forced Dissipated Yanai Beam. *J. Phys. Oceanogr.*, **40** (5), 1118–
658 1142, doi:10.1175/2010JPO4356.1.
- 659 Barnier, B., 1995: Thermal forcing for a global ocean circulation model using a three-year clima-
660 tology of ECMWF analyses. *J. Mar. Syst.*, **6**, 363–380.
- 661 Becker, J. J., D. T. Sandwell, W. H. F. Smith, and J. Braud, 2009: Global Bathymetry and Elevation
662 Data at 30 Arc Seconds Resolution : SRTM30 _ PLUS. *Mar. Geod.*, **32**:4, 355–371, doi:10.1080/
663 01490410903297766.
- 664 Beckmann, A., and D. B. Haidvogel, 1993: Numerical Simulation of Flow around a Tall Isolated
665 Seamount. Part I: Problem Formulation and Model Accuracy. *J. Phys. Oceanogr.*, **23**, 1736–
666 1753.
- 667 Carton, J. A., and B. S. Giese, 2008: A Reanalysis of Ocean Climate Using Simple Ocean Data
668 Assimilation (SODA). *J. Phys. Oceanogr.*, **136**, 2999–3017, doi:10.1175/2007MWR1978.1.
- 669 Conkright, M., R. A. Locarnini, H. Garcia, T. O'Brien, T. Boyer, C. Stephens, and J. Antonov,
670 2002: World Ocean Atlas 2001: Objective Analyses, Data Statistics, and Figures, CD-ROM

671 Documentation. Tech. Rep. September, National Oceanographic Data Center, Silver Spring,
672 MD., 17 pp.

673 Cox, M., 1980: Generation and propagation of 30-day waves in a numerical model of the pacific. *J.*
674 *Phys. Oceanogr.*, **10**, 1168–1186, doi:10.1175/1520-0485(1980)010<1168:GAPODW>2.0.CO;
675 2.

676 Cravatte, S., E. Kestenare, F. Marin, P. Dutrieux, and E. Firing, 2017: Subthermocline and In-
677 termediate Zonal Currents in the Tropical Pacific Ocean: Paths and Vertical Structure. *J. Phys.*
678 *Oceanogr.*, **47** (9), 2305–2324, doi:10.1175/JPO-D-17-0043.1.

679 Debreu, L., P. Marchesiello, P. Penven, and G. Cambon, 2012: Two-way nesting in split-explicit
680 ocean models: Algorithms, implementation and validation. *Ocean Model.*, **49-50**, 1–21, doi:
681 10.1016/j.ocemod.2012.03.003.

682 Delorme, B. L., and L. N. Thomas, 2019: Abyssal Mixing through Critical Reflection of
683 Equatorially Trapped Waves off Smooth Topography. *J. Phys. Oceanogr.*, **49**, 519–542, doi:
684 10.1175/JPO-D-18-0197.1.

685 Durland, T. S., and J. T. Farrar, 2012: The Wavenumber-Frequency Content of Resonantly Excited
686 Equatorial Waves. *J. Phys. Oceanogr.*, **42** (11), 1834–1858, doi:10.1175/JPO-D-11-0234.1.

687 Farrar, J. T., 2008: Observations of the Dispersion Characteristics and Meridional Sea Level
688 Structure of Equatorial Waves in the Pacific Ocean. *J. Phys. Oceanogr.*, **38** (8), 1669–1689,
689 doi:10.1175/2007JPO3890.1.

690 Farrar, J. T., and T. S. Durland, 2012: Wavenumber-Frequency Spectra of Inertia-Gravity and
691 Mixed Rossby-Gravity Waves in the Equatorial Pacific Ocean. *J. Phys. Oceanogr.*, **42** (11),
692 1859–1881, doi:10.1175/JPO-D-11-0235.1.

- 693 Ferrari, R., 2014: What goes down must come up. *Nature*, **513**, 179–180, doi:10.1038/513179a.
- 694 Gerkema, T., and V. I. Shrira, 2005: Near-inertial waves on the "nontraditional" beta-plane. *J.
695 Geophys. Res. Ocean.*, **110** (1), 1–10, doi:10.1029/2004JC002519.
- 696 Gerkema, T., J. T. Zimmerman, L. R. Maas, and H. Van Haren, 2008: Geophysical and astro-
697 physical fluid dynamics beyond the traditional approximation. *Rev. Geophys.*, **46** (2), 1–33,
698 doi:10.1029/2006RG000220, 0512217v1.
- 699 Gula, J., J. M. Molemaker, and J. C. McWilliams, 2015: Gulf Stream Dynamics along the South-
700 eastern U . S . Seaboard. *J. Phys. Oceanogr.*, **45**, 690–715, doi:10.1175/JPO-D-14-0154.1.
- 701 Holmes, R. M., J. N. Moum, and L. N. Thomas, 2016: Evidence for seafloor-intensified mixing
702 by surface-generated equatorial waves. *Geophys. Res. Lett.*, **43** (3), 1202–1210, doi:10.1002/
703 2015GL066472.
- 704 Jullien, S., and Coauthors, 2019: CROCO'S Technical and numerical Documentation. Tech. rep.,
705 CNRS-Ifremer-Inria-IRD-SHOM, 142 pp.
- 706 Kelly, B. G., S. D. Meyers, and J. J. O'Brien, 1995: On a generating mechanism for Yanai waves
707 and the 25-day oscillation. *J. Geophys. Res.*, **100**, 10 589–10 612.
- 708 Kessler, W. S., and J. P. McCreary, 1993: The Annual Wind-driven Rossby Wave in the
709 Subthermocline Equatorial Pacific. *J. Phys. Oceanogr.*, **23** (6), 1192–1207, doi:10.1175/
710 1520-0485(1993)023<1192:TAWDRW>2.0.CO;2.
- 711 Kindle, J. C., and J. D. Thompson, 1989: The 26- and 50-Day Oscillations in the Western Indian
712 Ocean ' Model Results. *J. Geophys. Res.*, **94**, 4721–4736.
- 713 Large, G. S., and W. G. Yeager, 2009: The global climatology of an interannually varying air –
714 sea flux data set. *Clim. Dyn.*, **33**, 341–364, doi:10.1007/s00382-008-0441-3.

- 715 Large, W. G., J. C. McWilliams, and S. C. Doney, 1994: Oceanic Vertical Mixing: a Review and
716 a Model with a Nonlocal Boundary-Layer Parameterization. *Rev. Geophys.*, **32** (94), 363–403,
717 doi:10.1029/94rg01872.
- 718 Lemarié, F., J. Kurian, A. F. Shchepetkin, M. Jeroen Molemaker, F. Colas, and J. C. McWilliams,
719 2012: Are there inescapable issues prohibiting the use of terrain-following coordinates in cli-
720 mate models? *Ocean Model.*, **42**, 57–79, doi:10.1016/j.ocemod.2011.11.007.
- 721 Lumpkin, R., and K. Speer, 2007: Global Ocean Meridional Overturning. *J. Phys. Oceanogr.*,
722 **37** (10), 2550–2562, doi:10.1175/JPO3130.1.
- 723 Lyman, J. M., G. C. Johnson, and W. S. Kessler, 2007: Distinct 17- and 33-Day Tropical Instability
724 Waves in Subsurface Observations. *J. Phys. Oceanogr.*, **37** (4), 855–872, doi:10.1175/JPO3023.
725 1.
- 726 Malardé, J.-P., P. De Mey, C. Périgaud, and J.-F. Minster, 1987: Observation of Long Equatorial
727 Waves in the Pacific Ocean by Seasat Altimetry. *J. Phys. Oceanogr.*, **17**, 2273–2279, doi:10.
728 1175/1520-0485-32.9.2715.
- 729 Marchesiello, P., J. C. McWilliams, and A. Shchepetkin, 2001: Open boundary conditions for
730 long-term integration of regional oceanic models. *Ocean Model.*, **3**, 1–20.
- 731 Marshall, J., C. Hill, L. Perelman, and A. Adcroft, 1997: Hydrostatic, quasi-hydrostatic, and
732 nonhydrostatic ocean modeling. *J. Geophys. Res.*, **102**, 5733–5752, doi:10.1029/96JC02776.
- 733 Mason, E., J. Molemaker, A. F. Shchepetkin, F. Colas, J. C. McWilliams, and P. Sangrà, 2010:
734 Procedures for offline grid nesting in regional ocean models. *Ocean Model.*, **35** (1-2), 1–15,
735 doi:10.1016/j.ocemod.2010.05.007, URL <http://dx.doi.org/10.1016/j.ocemod.2010.05.007>.

- 736 McPhaden, M. J., and R. A. Knox, 1979: Equatorial Kelvin and Inertio-Gravity Waves in Zonal
737 Shear Flow. *J. Phys. Oceanogr.*, **9**, 263–277.
- 738 Ménesguen, C., A. Delpech, F. Marin, S. Cravatte, and R. Schopp, 2019: Observations and Mecha-
739 nisms for the Formation of Deep Equatorial and Tropical Circulation. *Earth Sp. Sci.*, **6**, 370–386,
740 doi:10.1029/2018EA000438.
- 741 Molemaker, J. M., J. C. McWilliams, and W. K. Dewar, 2015: Submesoscale Instability and Gen-
742 eration of Mesoscale Anticyclones near a Separation of the California Undercurrent. *J. Phys.*
743 *Oceanogr.*, **45**, 613–629, doi:10.1175/JPO-D-13-0225.1.
- 744 Penven, P., and L. Debreu, 2006: Evaluation and application of the ROMS 1-way embedding
745 procedure to the central California upwelling system. *Ocean Model.*, **12**, 157–187, doi:10.1016/
746 j.ocemod.2005.05.002.
- 747 Polzin, K., J. Toole, J. R. Ledwell, and R. W. Schmitt, 1997: Spatial Variability of Turbulent
748 Mixing in the Abyssal Ocean. *Science (80-.).*, **276**, 93–96, doi:10.1126/science.276.5309.93.
- 749 Qiao, L., and R. H. Weisberg, 1995: Tropical instability wave kinematics: Observations from the
750 Tropical Instability Wave Experiments. *J. Geophys. Res.*, **100** (3), 8677–8693.
- 751 Risien, C. M., and D. B. Chelton, 2008: A global climatology of surface wind and wind stress
752 fields from eight years of QuikSCAT scatterometer data. *J. Phys. Oceanogr.*, **38** (11), 2379–
753 2413, doi:10.1175/2008JPO3881.1.
- 754 Shchepetkin, A. F., and J. C. McWilliams, 2005: The regional oceanic modeling system (ROMS):
755 A split-explicit, free-surface, topography-following-coordinate oceanic model. *Ocean Model.*,
756 **9** (4), 347–404, doi:10.1016/j.ocemod.2004.08.002.

- 757 Shchepetkin, A. F., and J. C. McWilliams, 2008: *Computational Kernel Algorithms for Fine-*
758 *Scale, Multiprocess, Longtime Oceanic Simulations*, Vol. 14. Elsevier B.V., 121–183 pp., doi:
759 10.1016/S1570-8659(08)01202-0, URL [http://dx.doi.org/10.1016/S1570-8659\(08\)01202-0](http://dx.doi.org/10.1016/S1570-8659(08)01202-0).
- 760 Shchepetkin, A. F., and J. C. McWilliams, 2009: Correction and commentary for “ Ocean fore-
761 casting in terrain-following coordinates : Formulation and skill assessment of the regional ocean
762 modeling system ” by Haidvogel et al ., *J . Comp . Phys .* 227 , pp . 3595 – 3624. *J. Comput.*
763 *Phys.*, **228 (24)**, 8985–9000, doi:10.1016/j.jcp.2009.09.002, URL <http://dx.doi.org/10.1016/j.jcp.2009.09.002>.
- 764 Shchepetkin, A. F., and J. C. McWilliams, 2011: Accurate Boussinesq oceanic modeling with
765 a practical , “ Stiffened ” Equation of State. *Ocean Model.*, **38 (1-2)**, 41–70, doi:10.1016/j.
766 ocemod.2011.01.010, URL <http://dx.doi.org/10.1016/j.ocemod.2011.01.010>.
- 767 Shinoda, T., 2012: Observation of first and second baroclinic mode Yanai waves in the ocean. *Q.*
768 *J. R. Meteorol. Soc.*, **138 (665)**, 1018–1024, doi:10.1002/qj.968.
- 769 Smith, W. H. F., and D. T. Sandwell, 1997: Global Sea Floor Topography from Satellite Altimetry
770 and Ship Depth Soundings. *Science (80-.).*, **277 (September)**, 1956–1962.
- 771 White, A. A., and R. A. Bromley, 1995: Dynamically consistent, quasi-hydrostatic equations for
772 global models with a complete representation of the Coriolis force. *Q. J. R. Meteorol. Soc.*,
773 **121 (522)**, 399–418, doi:10.1002/qj.49712152208.
- 774 Winters, K. B., P. Bouruet-Aubertot, and T. Gerkema, 2011: Critical reflection and abyssal trap-
775 ping of near-inertial waves on a beta-plane. *J. Fluid Mech.*, **684**, 111–136, doi:10.1017/jfm.
776 2011.280.

- 778 Woodberry, E., M. E. Luther, and J. O. Brien, 1989: The Wind-Driven Seasonal Circulation in the
- 779 Southern Tropical Indian Ocean. *J. Geophys. Res.*, **94**, 17,985–18,002.
- 780 Wunsch, C., and A. E. Gill, 1976: Observations of equatorially trapped waves in Pacific sea level
- 781 variations. *Deep. Res. Oceanogr. Abstr.*, **23 (5)**, 371–390, doi:10.1016/0011-7471(76)90835-4.

782 LIST OF FIGURES

- Fig. 1.** (a) Instantaneous sea surface temperature in the Pacific Basin at the beginning of December as simulated by ROMS. The parent domain covers most of the Pacific Ocean while the child domain is delineated by the thick grey lines (between 165°W and 105°W and $\pm 19^{\circ}\text{N}$). The Sea Surface Temperature plotted inside each of the domains is computed using data at their corresponding resolutions. In the eastern part of the basin, the surface signature of TIWs is clearly visible. (b) Seafloor bathymetry in the Eastern Equatorial Pacific taken from the SRTM30_PLUS dataset and used for the simulations. The bathymetry over most of the child domain is relatively smooth.

Fig. 2. Meridionally-averaged profiles of the stratification N^2 at 110°W between $\pm 2^{\circ}$ measured by Holmes et al. (2016) (orange line) and taken from the parent simulation (blue line) and the child simulations after a 1-year spin-up (the QH case is shown in purple, and the H case is shown in red). The stratification from all the independent casts available between 109 – 111°W and $\pm 2^{\circ}$ in the World Ocean Database 2013 is also shown (green line). The black dotted line represents the value of $\widetilde{f^2}$ at the equator. As shown in DT19, NT effects are expected to be stronger when $\Gamma = N^2/\widetilde{f^2} = O(1)$ or lower.

Fig. 3. Mean zonal currents averaged between 120–160°W (U) in the H (left) and QH (right) simulations. The averaged has been taken over the last 5 years of simulation.

Fig. 4. Wavenumber-frequency power spectrum of the meridional velocity in the H (left) and QH (right) simulations averaged over the surface σ -layer on the whole numerical domain of the child simulation and over the five years of simulation. Solid and dashed white lines are the theoretical dispersion curves for baroclinic modes 1 and 2, respectively, and are based on gravity wave speeds of 2.7 and 1.7 m/s, respectively.

Fig. 5. As in Figure 4 but for the meridional velocity averaged over the bottom σ -layer. The inertial latitude associated with each frequency is shown on the right y-axis. The horizontal dotted lines highlight the frequency and inertial latitudes of the waves that contribute the most to the enhanced shear in the QH run shown in Figure 10.

Fig. 6. The turbulent diffusivity averaged over the bottom 1000 m of the water column and over the five years of simulation in the H (top) and QH (bottom) runs. The black contour line in the bottom panel shows where $\Gamma = N/\widetilde{f} = 1$ at the bottom of the ocean over the bottom σ -layer. $\Gamma < 1$ within the contour lines where enhanced turbulent diffusivity is found.

Fig. 7. As in Figure 6 but for the vertical shear squared, $Sh^2 = (\frac{\partial u}{\partial z})^2 + (\frac{\partial v}{\partial z})^2$. The ratio between the QH and H case is shown in the bottom panel. The white contour line in the bottom panel shows where $\Gamma = N/\widetilde{f} = 1$ at the bottom of the ocean over the bottom σ -layer. $\Gamma < 1$ within the contour lines where enhanced vertical shear is found in the QH case.

Fig. 8. Turbulent diffusivity from the H (top) and QH (bottom) simulations at 130°W averaged over the five years of simulation.

Fig. 9. As in Figure 8 but for the vertical shear squared, $Sh^2 = (\frac{\partial u}{\partial z})^2 + (\frac{\partial v}{\partial z})^2$. The ratio between the QH and H case is shown in the bottom panel.

Fig. 10. Spectrum of the vertical shear in the bottom 500m of the water column from the H (left) and QH (right) simulations at 130°W as a function of latitude. The spectrum has been calculated over the five years of simulation. The plain white lines correspond to the inertial frequency.

The horizontal dotted lines highlight the frequency of the peaks in the spectrum of the shear in the QH run. The vertical magenta line indicates the latitude 5.5°S along which significant beams are found in Figure 11.

Fig. 11. Hovmöller diagram of time versus latitude of the vertical shear of the meridional velocity at 130°W for the three last months of the H (left) and QH (right) simulations at the bottom of the water column. The black dotted line shows the latitude 5.5°S along which the vertical profiles in Figure 12 were made. The pink arrows indicate the energy propagation of the beams.

Fig. 12. Hovmöller diagram of depth versus time of the vertical shear of the meridional velocity at 130°W and 5.5°S (corresponding to the black dotted line in the right panel of Figure 11) for the last three months of the H (top) and QH (bottom) simulations. The pink lines emphasize the vertical tilt in the phase of the beams.

Fig. 13. Schematic of the critical reflection mechanism. A downward-propagating ETW transmits energy on the steep characteristic, which has a slope $\mu_{\omega=f}^{+}$. At a flat boundary, ray tubes are compressed to an infinitesimally small layer resulting in an amplification of the reflected IGW at the inertial latitude of the wave. The blue and red contours are depicting the phase of the wave.

Fig. 14. Variance of the surface meridional velocity bandpass filtered around the frequency of six ETWs seen in Figures 4 and 5: the 33-day Rossby wave, the 23-day Yanai wave, the 17-day Yanai wave, the 6-day IGW, the 5-day IGW and the 3-day IGW.

Fig. 15. Ray paths of the six ETW types in Figure 14. For each wave, 20 rays are fired from the surface. The frequency and zonal wavenumber of the waves are chosen randomly within a range corresponding to each wave type. Similarly, the starting longitude of the wave is chosen randomly within an area corresponding to enhanced surface velocity variance for each wave (shown in Figure 14). The number between parenthesis next to the name of the wave corresponds to the average time in days it takes for the wave to reach the bottom from the surface.

Fig. 16. Ratio of the slope of the steep characteristic at the inertial latitude, $\mu_{\omega=f}^{+}$ (as defined in Figure 13), to the slope of the seafloor in the meridional direction, $s = \frac{\partial h}{\partial y}$, where h is the depth of the water column. When this ratio is large, the critical reflection mechanism due to NT effects is more efficient.

Fig. 17. Characteristic curves $\xi_{\pm} = \mu^{\pm}y - z$ (in blue and red), phase velocity vectors (in green) and group velocity vectors (in orange) for an inertia-gravity wave propagating over an f -plane with constant stratification in the NT case in the superinertial ($\omega > f$, right), inertial ($\omega = f$, center) and subinertial ($\omega < f$, right) regimes (where ω the frequency of the wave).

Fig. 18. Histogram of the buoyancy frequency in the bottom 1000 m of the water column with the mean (plain white line), median (dashed white line) and 10th percentile (dotted white line) of the distribution plotted as a function of latitude (left) and longitude (right) for the H (top) and QH (bottom) runs. The pink line represents the value of \tilde{f}^2

Fig. 19. Histogram of the diapycnal vertical velocity in the bottom 1000 m of the water column with the mean of the distribution (pink line) plotted as a function of latitude (left) and longitude (right) for the H (top) and QH (bottom) runs.

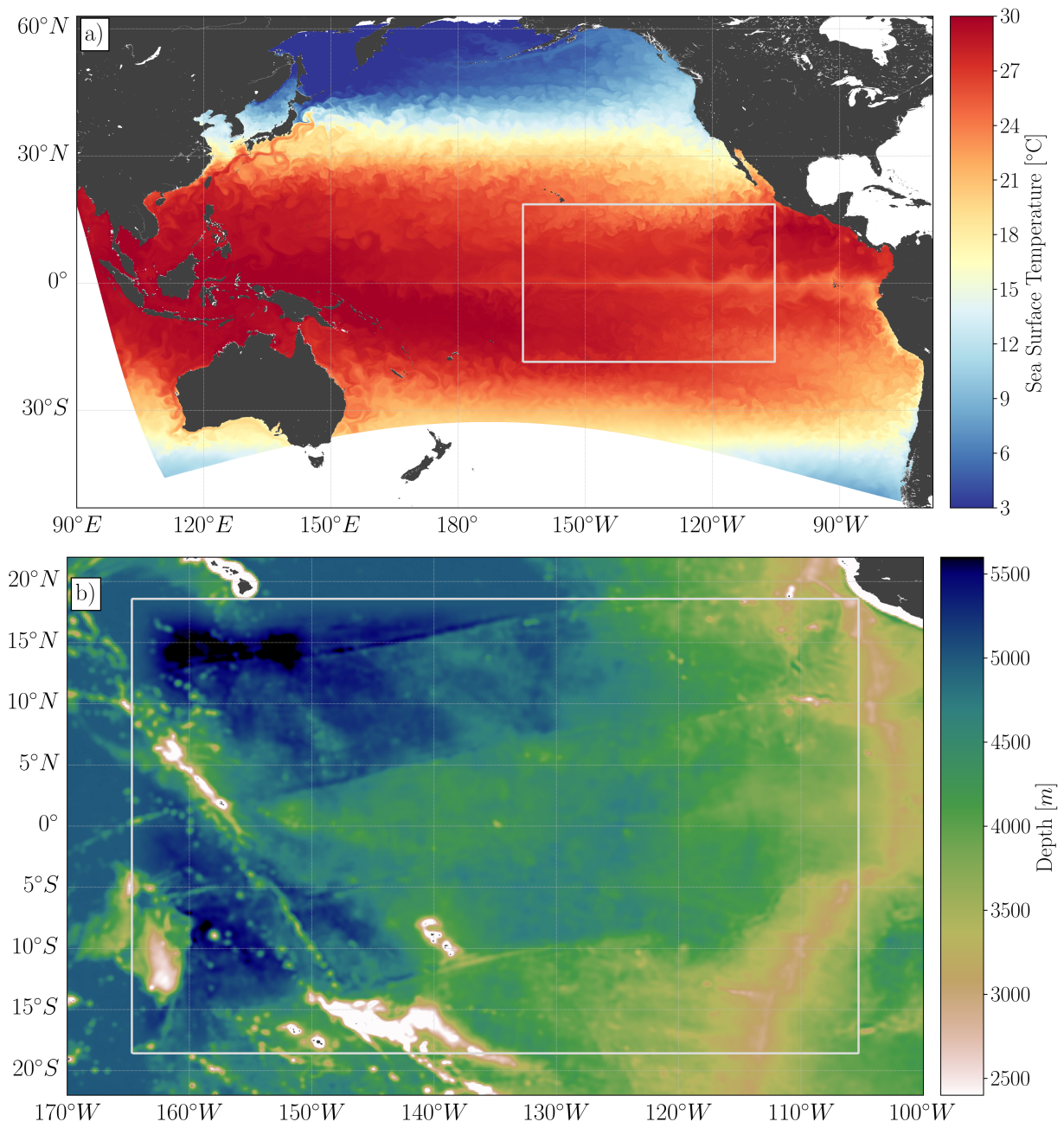
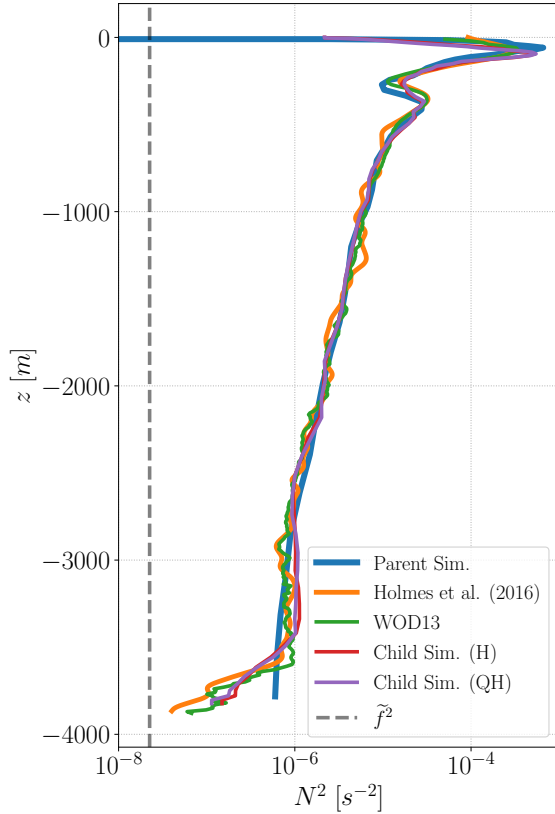


FIG. 1. (a) Instantaneous sea surface temperature in the Pacific Basin at the beginning of December as simulated by ROMS. The parent domain covers most of the Pacific Ocean while the child domain is delineated by the thick grey lines (between 165°W and 105°W and $\pm 19^{\circ}\text{N}$). The Sea Surface Temperature plotted inside each of the domains is computed using data at their corresponding resolutions. In the eastern part of the basin, the surface signature of TIWs is clearly visible. (b) Seafloor bathymetry in the Eastern Equatorial Pacific taken from the SRTM30_PLUS dataset and used for the simulations. The bathymetry over most of the child domain is relatively smooth.



876 FIG. 2. Meridionally-averaged profiles of the stratification N^2 at $110^\circ W$ between $\pm 2^\circ$ measured by Holmes
 877 et al. (2016) (orange line) and taken from the parent simulation (blue line) and the child simulations after a
 878 1-year spin-up (the QH case is shown in purple, and the H case is shown in red). The stratification from all the
 879 independent casts available between $109 - 111^\circ W$ and $\pm 2^\circ$ in the World Ocean Database 2013 is also shown
 880 (green line). The black dotted line represents the value of \tilde{f}^2 at the equator. As shown in DT19, NT effects are
 881 expected to be stronger when $\Gamma = N^2/\tilde{f}^2 = O(1)$ or lower.

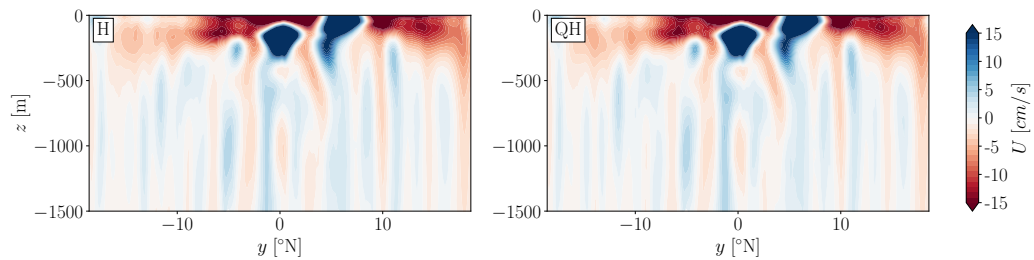
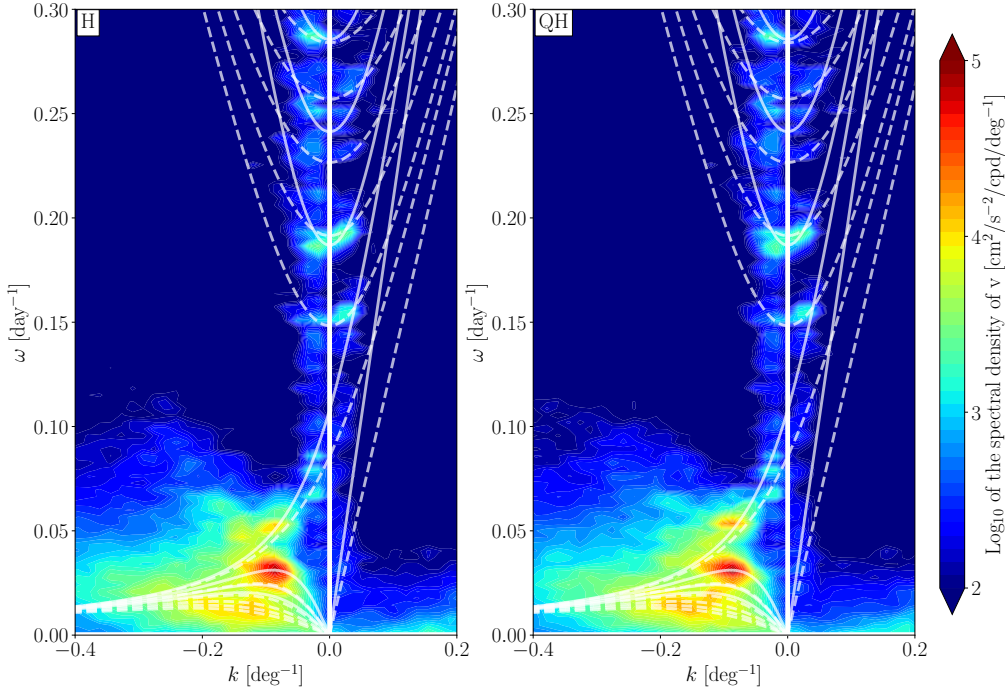
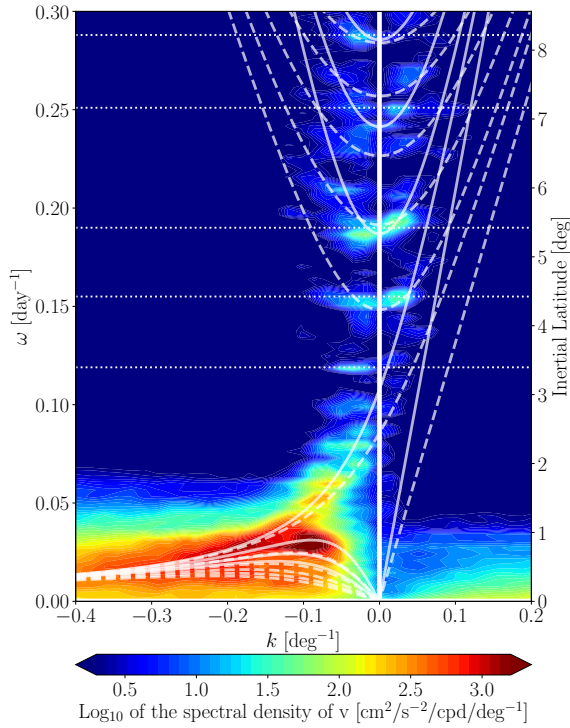


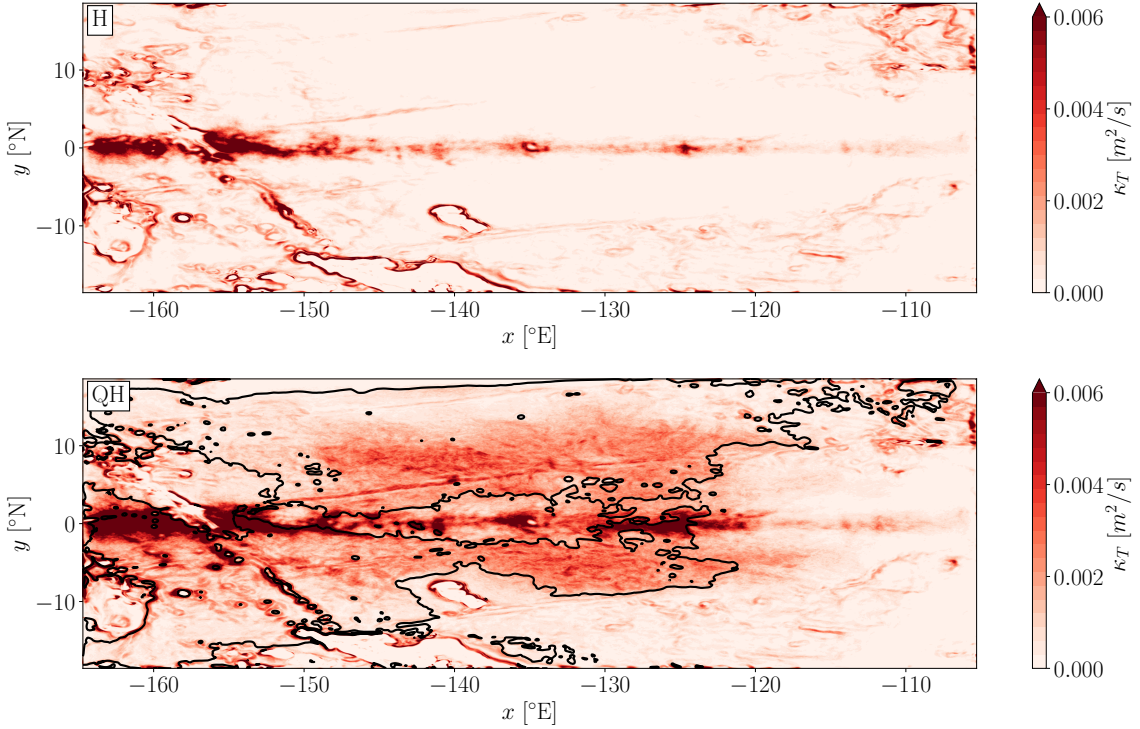
FIG. 3. Mean zonal currents averaged between $120\text{--}160^\circ\text{W}$ (U) in the H (left) and QH (right) simulations.
 The averaged has been taken over the last 5 years of simulation.



884 FIG. 4. Wavenumber-frequency power spectrum of the meridional velocity in the H (left) and QH (right)
 885 simulations averaged over the surface σ —layer on the whole numerical domain of the child simulation and over
 886 the five years of simulation. Solid and dashed white lines are the theoretical dispersion curves for baroclinic
 887 modes 1 and 2, respectively, and are based on gravity wave speeds of 2.7 and 1.7 m/s, respectively.



888 FIG. 5. As in Figure 4 but for the meridional velocity averaged over the bottom σ -layer. The inertial latitude
 889 associated with each frequency is shown on the right y-axis. The horizontal dotted lines highlight the frequency
 890 and inertial latitudes of the waves that contribute the most to the enhanced shear in the QH run shown in Figure
 891 10.



892 FIG. 6. The turbulent diffusivity averaged over the bottom 1000 m of the water column and over the five
 893 years of simulation in the H (top) and QH (bottom) runs. The black contour line in the bottom panel shows
 894 where $\Gamma = N/\tilde{f} = 1$ at the bottom of the ocean over the bottom σ -layer. $\Gamma < 1$ within the contour lines where
 895 enhanced turbulent diffusivity is found.

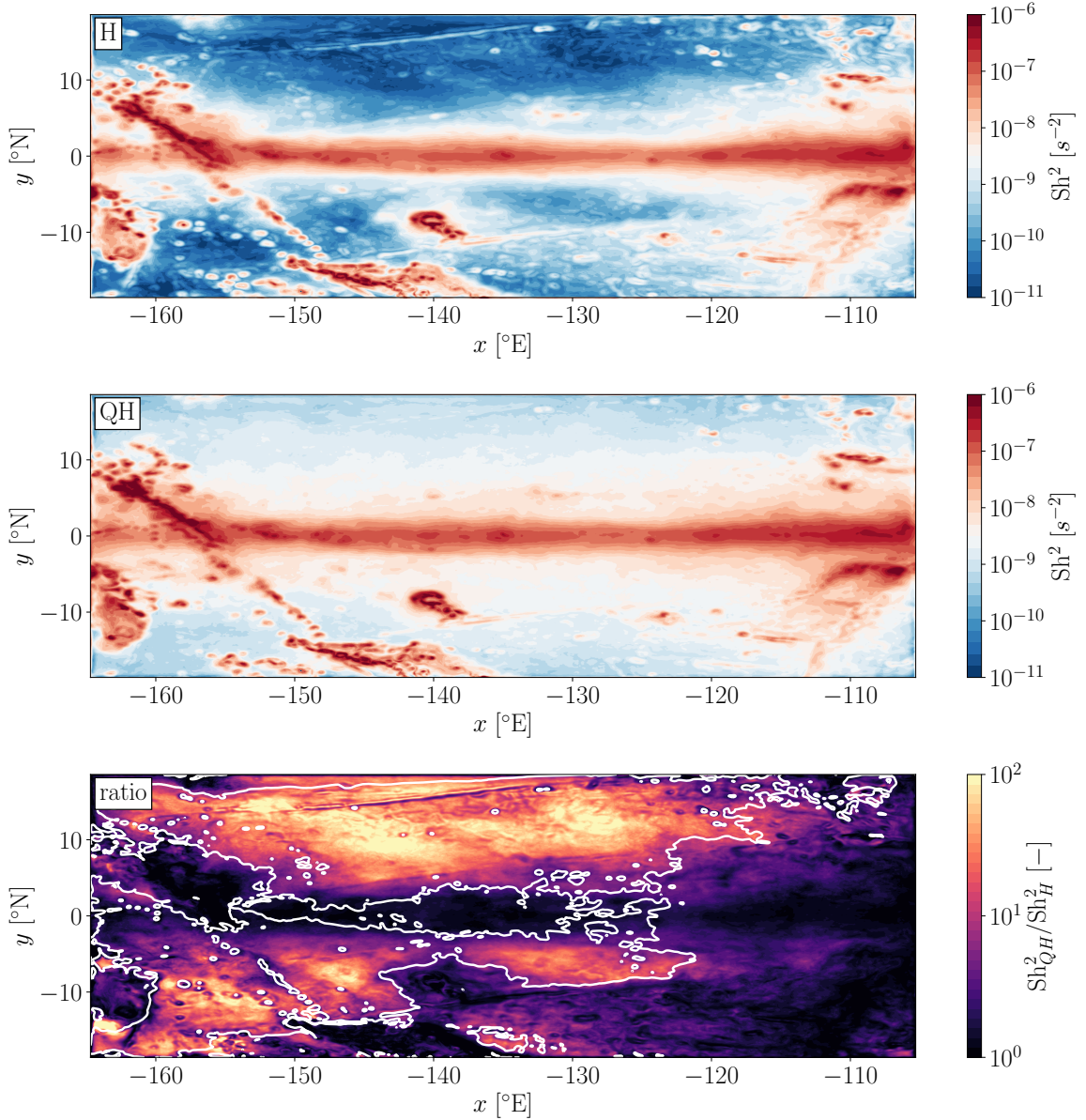
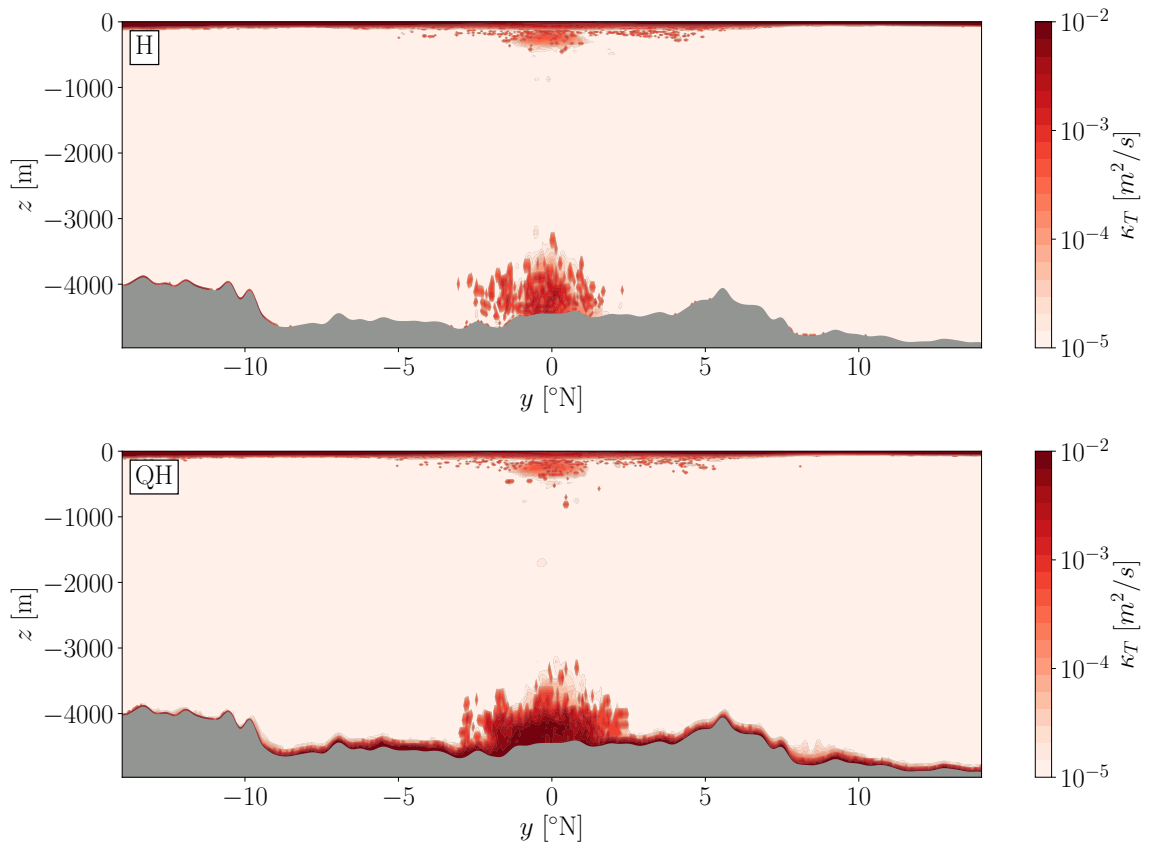
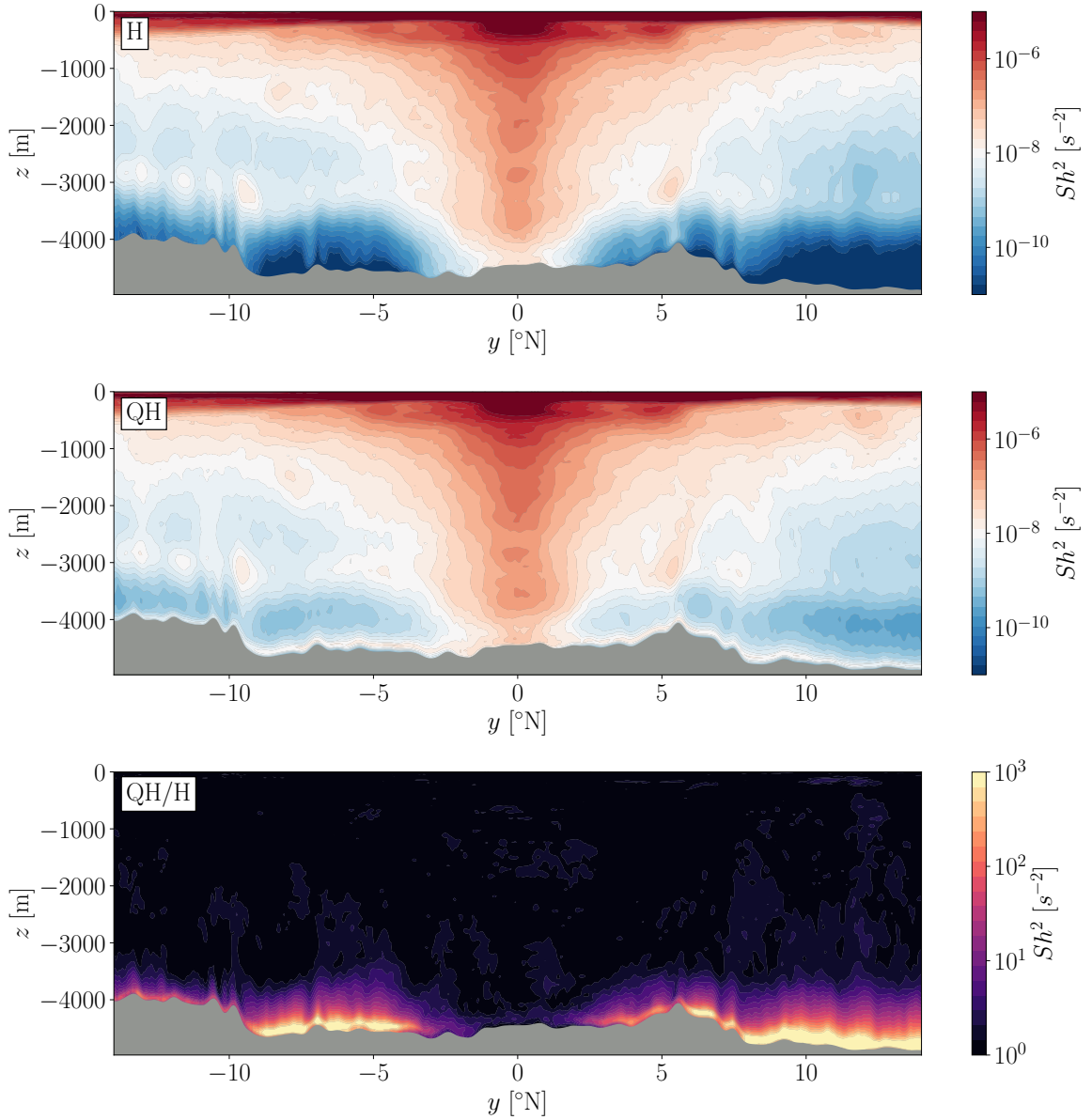


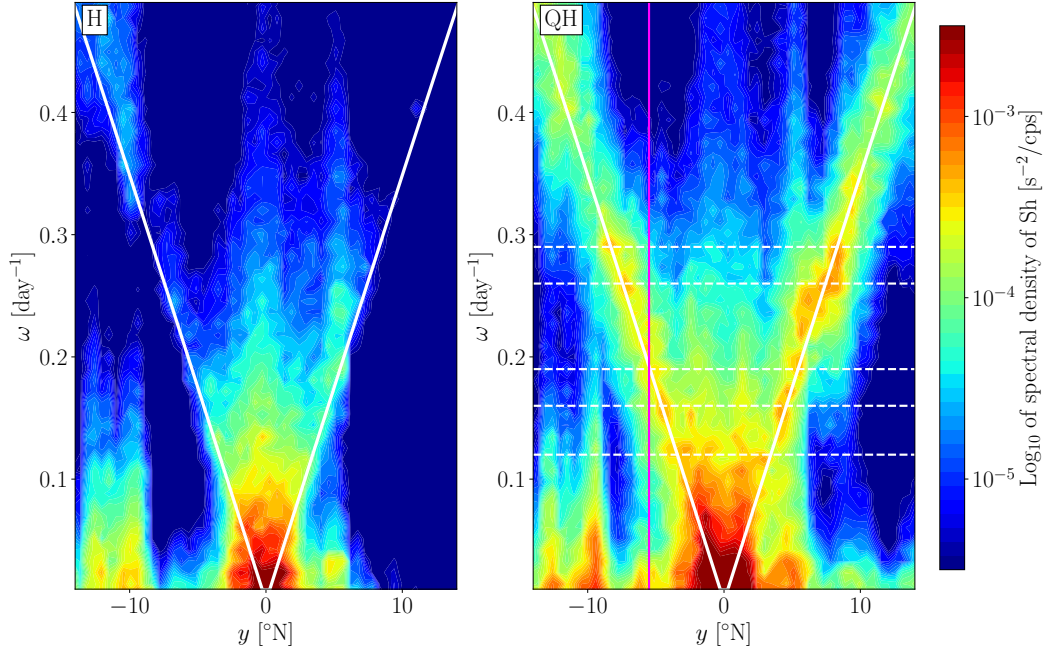
FIG. 7. As in Figure 6 but for the vertical shear squared, $Sh^2 = (\frac{\partial u}{\partial z})^2 + (\frac{\partial v}{\partial z})^2$. The ratio between the QH and H case is shown in the bottom panel. The white contour line in the bottom panel shows where $\Gamma = N/\tilde{f} = 1$ at the bottom of the ocean over the bottom σ -layer. $\Gamma < 1$ within the contour lines where enhanced vertical shear is found in the QH case.



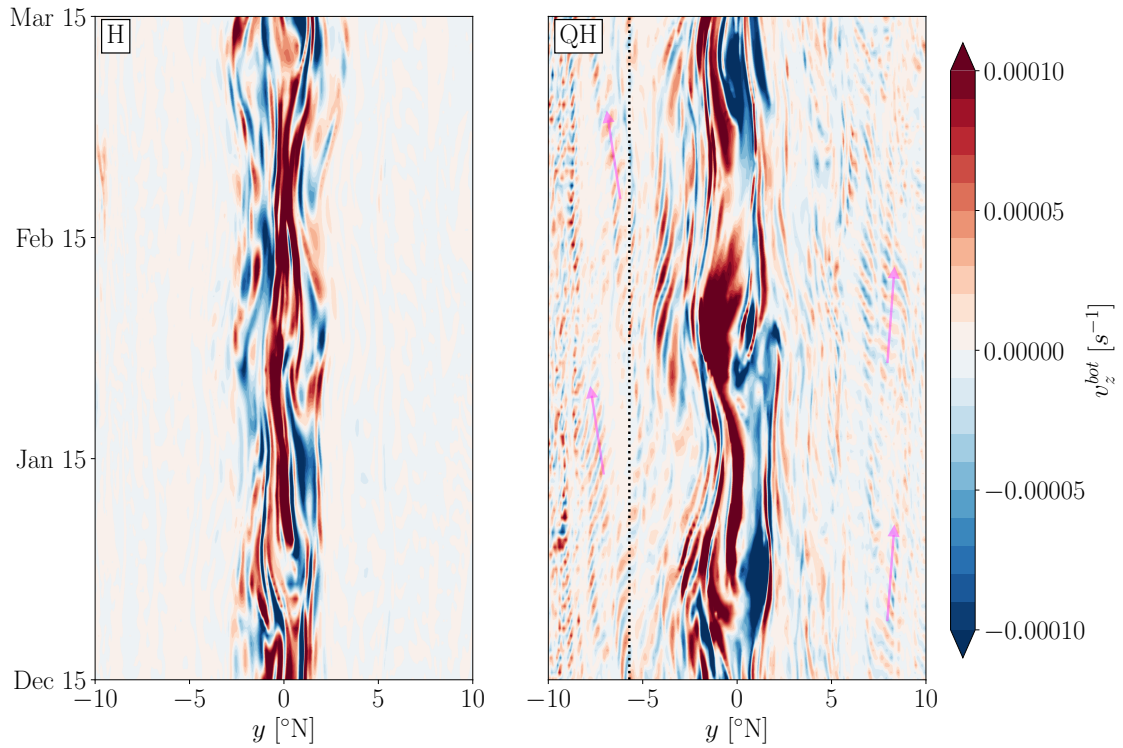
900 FIG. 8. Turbulent diffusivity from the H (top) and QH (bottom) simulations at 130°W averaged over the five
901 years of simulation.



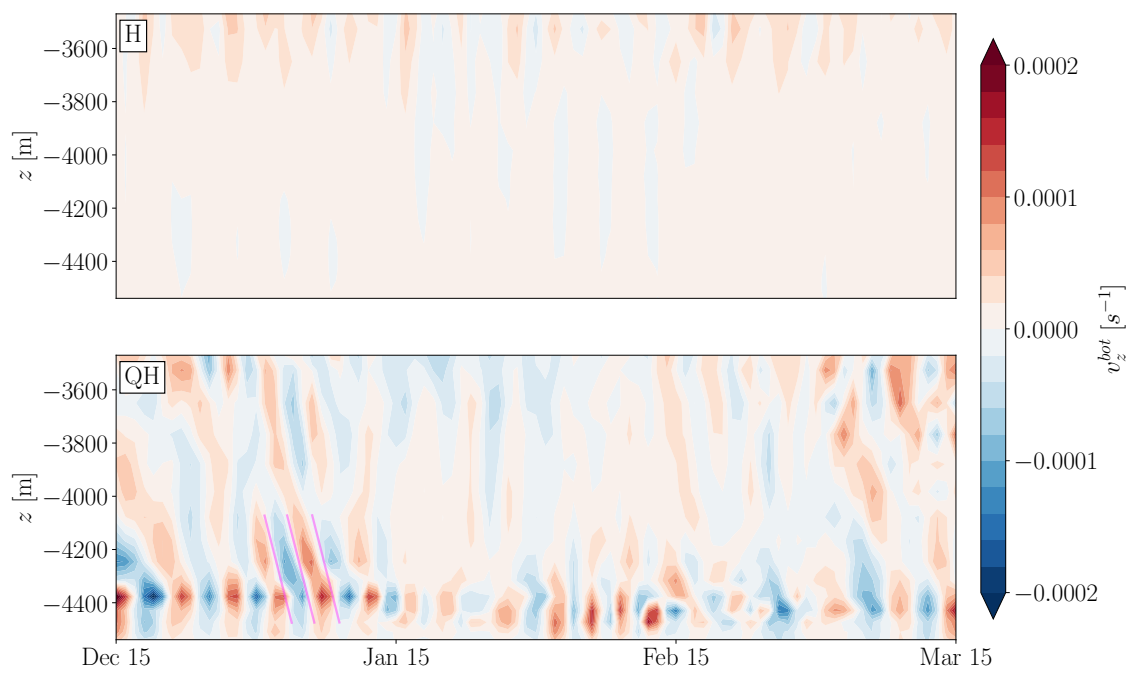
902 FIG. 9. As in Figure 8 but for the vertical shear squared, $Sh^2 = (\frac{\partial u}{\partial z})^2 + (\frac{\partial v}{\partial z})^2$. The ratio between the QH and
903 H case is shown in the bottom panel.



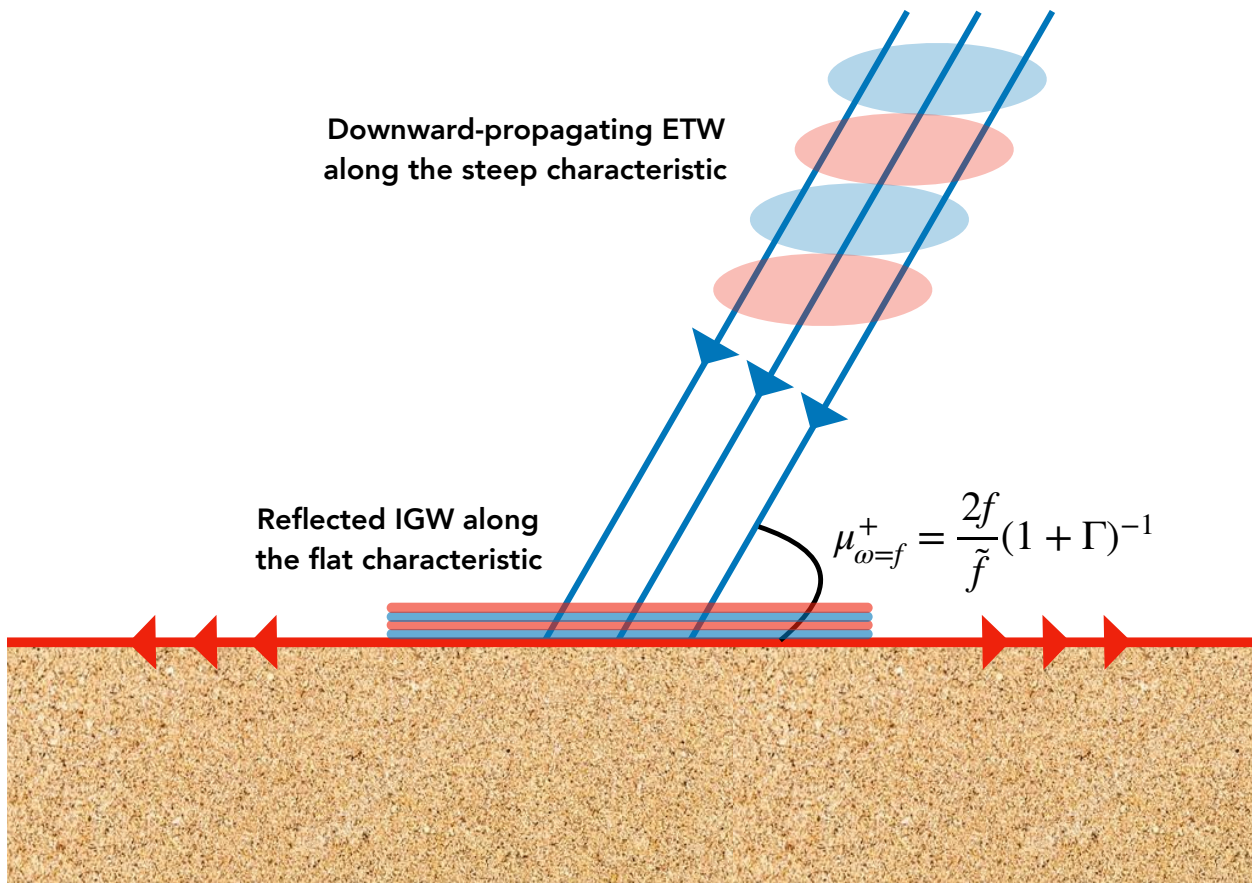
904 FIG. 10. Spectrum of the vertical shear in the bottom 500m of the water column from the H (left) and QH
905 (right) simulations at 130°W as a function of latitude. The spectrum has been calculated over the five years
906 of simulation. The plain white lines correspond to the inertial frequency. The horizontal dotted lines highlight
907 the frequency of the peaks in the spectrum of the shear in the QH run. The vertical magenta line indicates the
908 latitude 5.5°S along which significant beams are found in Figure 11.



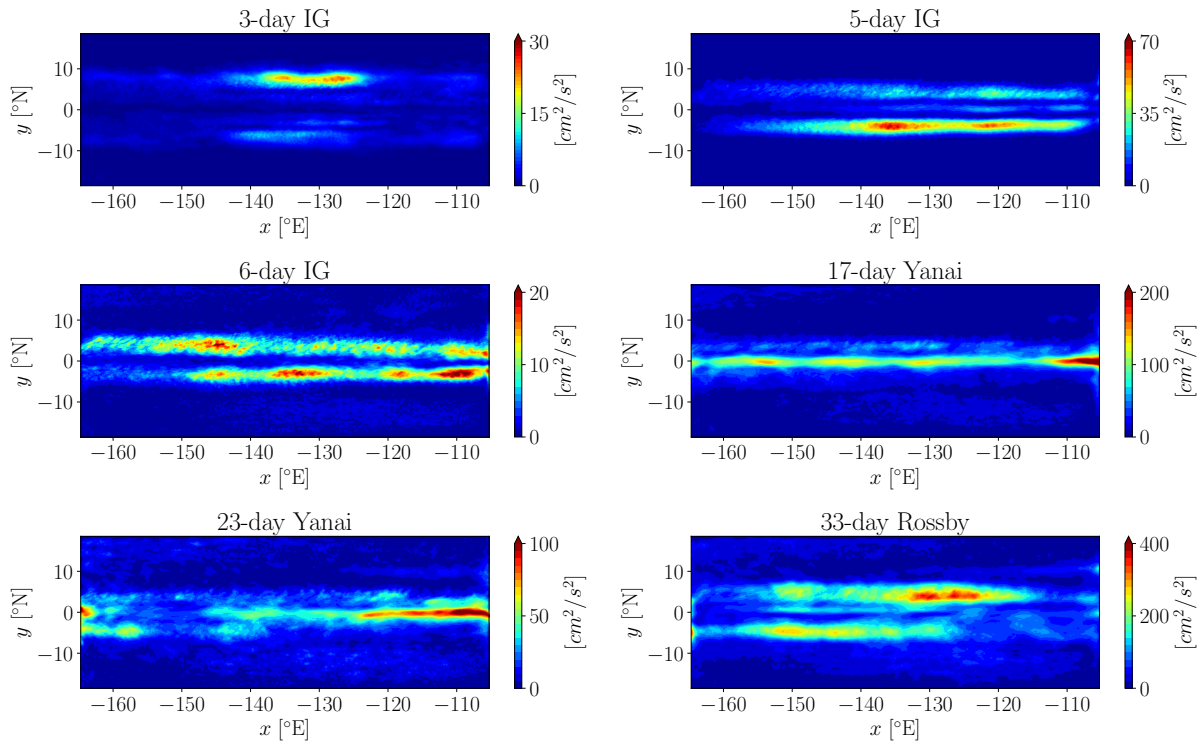
909 FIG. 11. Hovmöller diagram of time versus latitude of the vertical shear of the meridional velocity at 130°W
 910 for the three last months of the H (left) and QH (right) simulations at the bottom of the water column. The black
 911 dotted line shows the latitude 5.5°S along which the vertical profiles in Figure 12 were made. The pink arrows
 912 indicate the energy propagation of the beams.



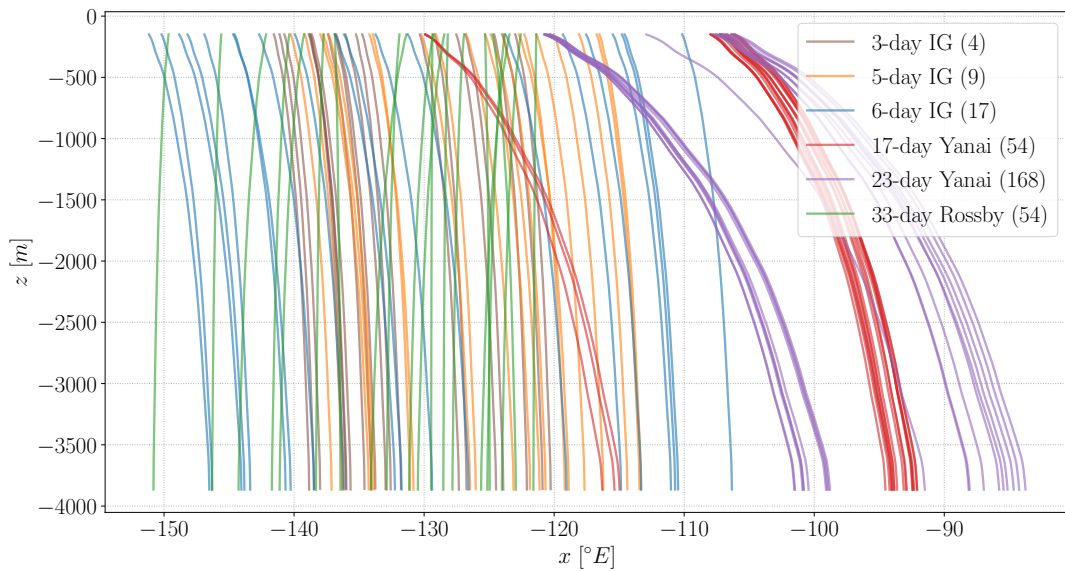
913 FIG. 12. Hovmöller diagram of depth versus time of the vertical shear of the meridional velocity at 130°W
 914 and 5.5°S (corresponding to the black dotted line in the right panel of Figure 11) for the last three months of the
 915 H (top) and QH (bottom) simulations. The pink lines emphasize the vertical tilt in the phase of the beams.



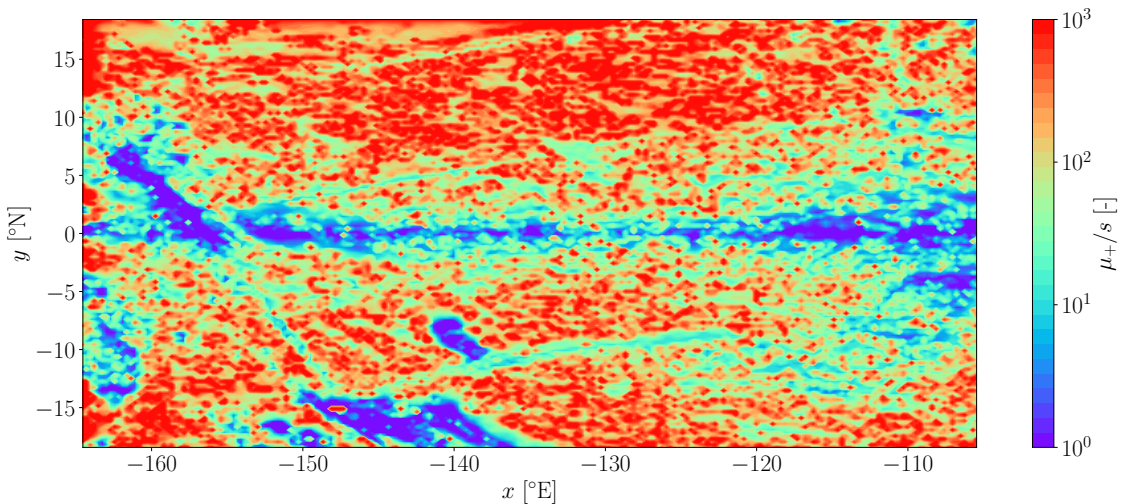
916 FIG. 13. Schematic of the critical reflection mechanism. A downward-propagating ETW transmits energy on
 917 the steep characteristic, which has a slope $\mu_{\omega=f}^+$. At a flat boundary, ray tubes are compressed to an infinitesi-
 918 mally small layer resulting in an amplification of the reflected IGW at the inertial latitude of the wave. The blue
 919 and red contours are depicting the phase of the wave.



920 FIG. 14. Variance of the surface meridional velocity bandpass filtered around the frequency of six ETWs seen
 921 in Figures 4 and 5: the 33-day Rossby wave, the 23-day Yanai wave, the 17-day Yanai wave, the 6-day IGW, the
 922 5-day IGW and the 3-day IGW.



923 FIG. 15. Ray paths of the six ETW types in Figure 14. For each wave, 20 rays are fired from the surface. The
 924 frequency and zonal wavenumber of the waves are chosen randomly within a range corresponding to each wave
 925 type. Similarly, the starting longitude of the wave is chosen randomly within an area corresponding to enhanced
 926 surface velocity variance for each wave (shown in Figure 14). The number between parenthesis next to the name
 927 of the wave corresponds to the average time in days it takes for the wave to reach the bottom from the surface.



928 FIG. 16. Ratio of the slope of the steep characteristic at the inertial latitude, $\mu_{\omega=f}^+$ (as defined in Figure 13),
 929 to the slope of the seafloor in the meridional direction, $s = \frac{\partial h}{\partial y}$, where h is the depth of the water column. When
 930 this ratio is large, the critical reflection mechanism due to NT effects is more efficient.

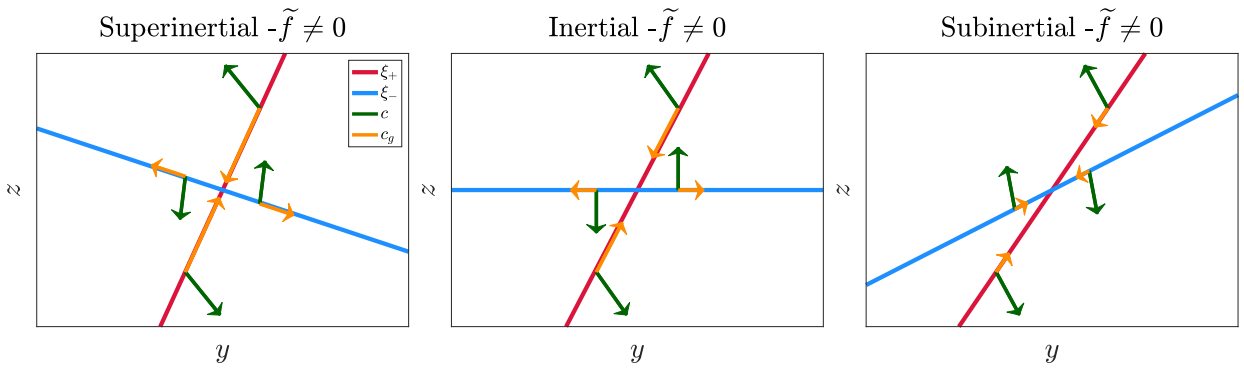
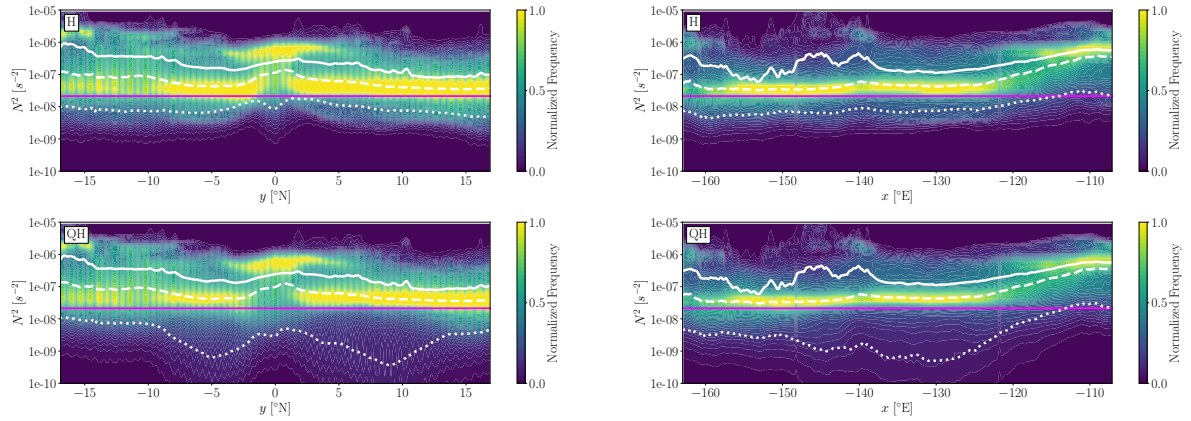
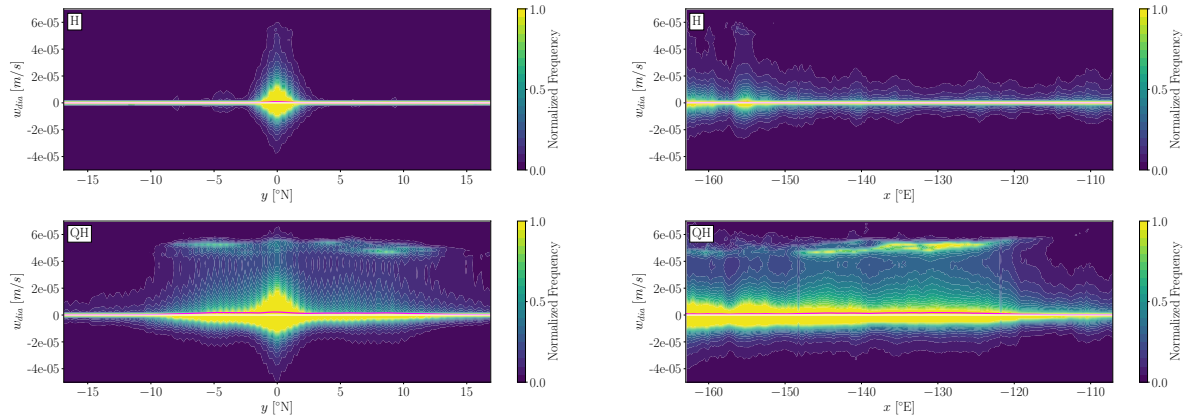


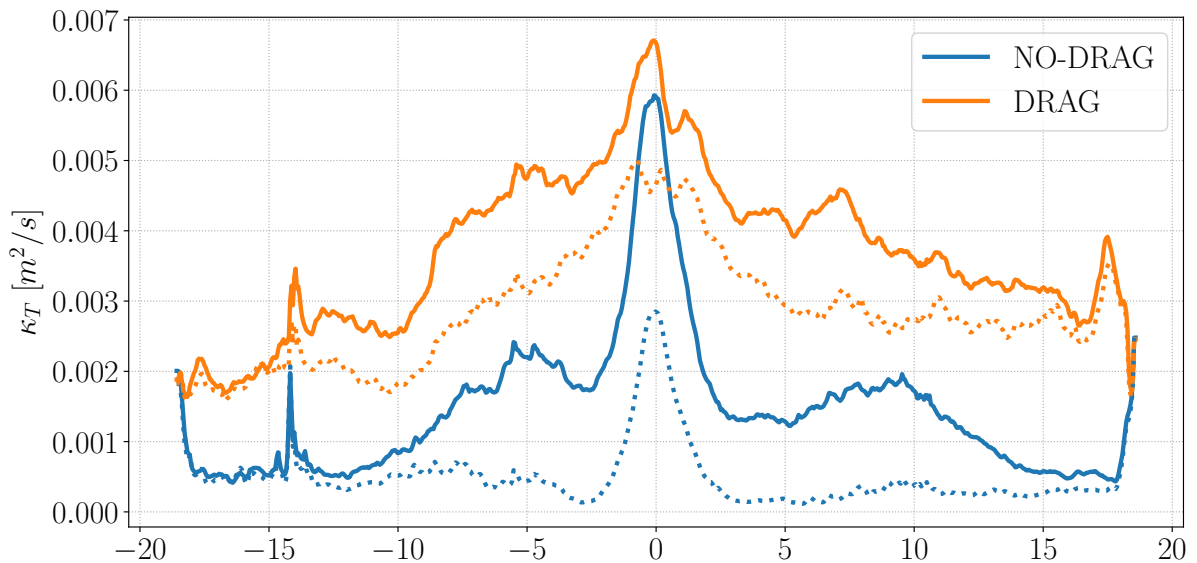
FIG. 17. Characteristic curves $\xi_{\pm} = \mu^{\pm}y - z$ (in blue and red), phase velocity vectors (in green) and group velocity vectors (in orange) for an inertia-gravity wave propagating over an f -plane with constant stratification in the NT case in the superinertial ($\omega > f$, right), inertial ($\omega = f$, center) and subinertial ($\omega < f$, right) regimes (where ω the frequency of the wave).



935 FIG. 18. Histogram of the buoyancy frequency in the bottom 1000 m of the water column with the mean (plain
 936 white line), median (dashed white line) and 10th percentile (dotted white line) of the distribution plotted as a
 937 function of latitude (left) and longitude (right) for the H (top) and QH (bottom) runs. The pink line represents
 938 the value of \tilde{f}^2 .



939 FIG. 19. Histogram of the diapycnal vertical velocity in the bottom 1000 m of the water column with the
 940 mean of the distribution (pink line) plotted as a function of latitude (left) and longitude (right) for the H (top)
 941 and QH (bottom) runs.



942 FIG. 20. The turbulent diffusivity averaged over the bottom 1000 m of the water column, over all longitudes
 943 and over the five years of simulation in the H (dotted lines) and QH (plain lines) runs with (orange) and without
 944 (blue) bottom drag.